



Trends and drivers of soluble iron deposition from East Asian dust to the Northwest Pacific: a springtime analysis (2001–2017)

Hanzheng Zhu^{1,2,3}, Yaman Liu^{1,4}, Man Yue^{1,4}, Shihui Feng⁵, Pingqing Fu⁵, Kan Huang⁶,
Xinyi Dong^{1,2,3}, and Minghuai Wang^{1,3}

¹School of Atmospheric Science, Nanjing University, Nanjing, 210023, China

²Frontiers Science Center for Critical Earth Material Cycling, Nanjing University, Nanjing, 210023, China

³Joint International Research Laboratory of Atmospheric and Earth System Sciences & Institute for Climate and Global Change Research, Nanjing University, Nanjing, 210023, China

⁴Laboratory of Atmospheric Composition and Climate Change,

Zhejiang Institute of Meteorological Sciences, Hangzhou, 310008, China

⁵Institute of Surface-Earth System Science, School of Earth System Science,
Tianjin University, Tianjin, 300072, China

⁶Department of Environmental Science and Engineering, Fudan University, Shanghai, 200433, China

Correspondence: Xinyi Dong (dongxy@nju.edu.cn)

Received: 21 July 2024 – Discussion started: 22 October 2024

Revised: 2 February 2025 – Accepted: 24 February 2025 – Published: 21 May 2025

Abstract. Recent shifts in dust emissions and atmospheric compositions in East Asia may have a significant impact on the deposition of soluble iron from dust over the Northwest Pacific (30–50° N, 140° E–160° W). This study investigates the trends and driving factors behind this phenomenon during the spring of 2001–2017 using an enhanced version of the Community Atmosphere Model version 6 with comprehensive stratospheric chemistry (CAM6-Chem). We improved the model to account for desert dust mineralogy and atmospheric chemical processes that promote iron dissolution, allowing for an in-depth analysis of the evolution of dust iron. Our findings indicate a decreasing trend in dust-soluble-iron deposition from East Asia to the Northwest Pacific by 2.4 % yr⁻¹, primarily due to reduced dust emissions driven by declining surface winds over dust source regions. Conversely, the solubility of dust iron showed an increasing trend, rising from 1.5 % in 2001 to 1.7 % in 2017. This increased iron solubility is linked to the acidification of coarse-mode aerosols and in-cloud oxalate-promoted dissolution. Sensitivity model simulations reveal that the increase in anthropogenic NO_x emissions, rather than the decrease in SO₂, plays a dominant role in enhancing dust aerosol acidity. This study highlights a dual trend: a decrease in the overall deposition of soluble iron from dust but an increase in the solubility of the iron itself. It underscores the critical roles of both dust emission and atmospheric processing in promoting iron dissolution, which further influences soluble iron deposition and marine ecology.

1 Introduction

Dust aerosols profoundly influence the Earth's system (Kok et al., 2023) by absorbing and scattering radiation (Kok et al., 2017; Li et al., 2021), acting as cloud condensation nuclei (Karydis et al., 2017; Storelvmo, 2017), and providing essential nutrients to oceanic ecosystems (Mahowald, 2011). Among these impacts, the role of dust as a transporter of iron is particularly noteworthy due to its significant influence on marine productivity (Meskhidze et al., 2005; Jickells et al., 2005). The limited availability of iron constrains biological productivity in vast expanses of the ocean, particularly in high-nutrient, low-chlorophyll (HNLC) regions (Martin, 1990; Martin et al., 1991). The deposition of iron-rich dust into the ocean acts as a much-needed nutrient source, catalyzing the growth of phytoplankton (Hettiarachchi et al., 2021). The stimulation of phytoplankton growth not only boosts marine productivity but also has broader implications for carbon sequestration (Jickells et al., 2014). Understanding the dynamics of dust-borne iron deposition is critically important for comprehending and predicting changes in marine ecosystems and global climate (Jickells and Moore, 2015).

During atmospheric transport, atmospheric processing may significantly modify the bioavailability (solubility) of dust iron, which is a critical factor for marine phytoplankton uptake. Observational studies have indicated that dust iron solubility could increase from as low as 2 % to up to nearly 10 % (Longo et al., 2016). The increase is primarily attributed to two atmospheric processes (Shi et al., 2012). The first involves interactions between dust aerosols and acidic gases or aerosols, leading to higher hydrogen ion concentrations that facilitate the dissolution of iron (Shi et al., 2011; Zhu et al., 2020). The second encompasses the formation of soluble iron-organic complexes, particularly through dust interactions with organic compounds like oxalate (Reichard et al., 2005; Paris and Desboeufs, 2013). Previous studies have simulated the atmospheric processing of dust iron by different models such as IMPACT (Ito and Xu, 2014; Ito, 2015; Ito and Feng, 2010), EC-Earth (Myriokefalitakis et al., 2022), GEOS-Chem (Johnson and Meskhidze, 2013), and CESM (Scanza et al., 2018; Hamilton et al., 2019) and indicated that these processes may play an important role in altering the solubility of dust iron. However, the long-term trend of soluble iron due to the rapid changes in both natural dust emissions and anthropogenic emissions (Hamilton et al., 2020; Bergas-Massó et al., 2023) in recent decades remains poorly documented.

East Asia has two major dust emission sources: the Taklimakan and Gobi deserts, which account for 14 % of global dust emissions (Kok et al., 2023). It also has intensive anthropogenic emissions, which may result in increased iron solubility through the long-range transport of dust. Influenced by prevailing westerlies and monsoonal patterns, dust from East Asia could supply significant amounts of bioavailable iron to the Northwest Pacific (30–50° N, 140° E–160° W) and

induce a substantial impact (Guo et al., 2017; Zan et al., 2023). Among the global HNLC regions which are the subarctic Pacific, the equatorial Pacific, and the Southern Ocean, the subarctic Pacific stands out due to its high sensitivity to iron fertilization (Martin and Fitzwater, 1988; Takeda and Tsuda, 2005). In recent decades, significant changes in natural mineral dust and anthropogenic emissions (Wu et al., 2022; Zheng et al., 2018) have necessitated a thorough evaluation of the contribution of East Asian dust to soluble iron deposition in the Northwest Pacific. Consequently, it is crucial to understand the trend and the driving factors to assess the impact accurately and develop informed environmental management strategies, and modeling is one of the best methods for this evaluation.

In this study, we aim to better understand the long-term trend and driving factors of dust-soluble-iron deposition from East Asia to the Northwest Pacific using an advanced model. We improved a global chemical–climate model to simulate the total and soluble dust iron emissions, transport, and deposition. Based on the simulation results, we quantified the interannual trend in dust-soluble-iron deposition during spring from 2001 to 2017, considering contributions from both initial emissions and atmospheric processing, which include proton-promoted and oxalate-promoted processes. Sensitivity experiments were conducted to explore the impact of anthropogenic emissions on dust-soluble-iron deposition in the Northwest Pacific. We also demonstrated a positive response from phytoplankton to dust-soluble-iron deposition by combining simulated high dust-soluble-iron depositions with satellite-derived sea surface chlorophyll concentrations.

2 Data and methods

2.1 Model platform

Utilizing the Community Atmosphere Model version 6 with comprehensive stratospheric chemistry (CAM6-Chem), our study simulated the atmospheric dynamics of dust iron aerosols (Danabasoglu et al., 2020). Dust emissions are generated through the Dust Entrainment and Deposition (DEAD) model, utilizing a geomorphic source function to accurately represent global soil erodibility variations (Zender et al., 2003a, b). The model categorizes dust aerosols into three sizes: Aitken (0.01–0.1 µm), accumulation (0.1–1.0 µm), and coarse (1.0–10.0 µm), with specific geometric standard deviations at 1.6, 1.6, and 1.2 for each (Liu et al., 2016). Following the brittle fragmentation theory, the mass fractions of dust aerosol are configured to be 0.00165 %, 1.1 %, and 98.9 % for each mode respectively (Kok, 2011).

To refine atmospheric iron aerosol processing, we employed an updated CAM version coupled with the Model for Simulating Aerosol Interactions and Chemistry (MO-SAIC) (Zaveri et al., 2021). In CAM6-Chem, secondary organic aerosol (SOA) formation follows a Volatility Basis Set (VBS) approach with explicit volatile organic compounds

(VOCs) and chemistry (Emmons et al., 2020; Tilmes et al., 2019). It incorporates wall-corrected SOA yields, photolytic removal of SOA, and more efficient removal by dry and wet deposition. What is more, the heterogeneous uptake of isoprene epoxydiols (IEPOX) onto sulfate aerosols and their subsequent production are explicitly simulated through coupling with MOSAIC (Jo et al., 2019, 2021). MOSAIC simulates the heterogeneous chemical processes on dust and is skilled at calculating size-resolved aerosol pH, which has been widely used to explore aerosols' impact on air quality, climate, and health (Ruan et al., 2022; Liu et al., 2023). Firstly, the MOSAIC mechanism would determine whether the aerosol contains solid CaCO_3 , which can adsorb acidic gases (H_2SO_4 , HNO_3 , and HCl). The irreversible heterogeneous reactions which would consume solid CaCO_3 are listed in Table S1. Before CaCO_3 was consumed, the aerosol pH was dependent on the hydrogen ions dissociated from water instead of acids (Zaveri et al., 2008). This process was influenced by temperature (T) (in units of K) as follows (Eq. 1):

$$\text{pH} = \sqrt{1.01^{-14} e^{-22.52\left(\frac{1}{T}-1\right)+26.92\left(1+\log_{10}\left(\frac{1}{T}\right)-\frac{1}{T}\right)}}. \quad (1)$$

After CaCO_3 was consumed, the MOSAIC defined two domains (sulfate-rich and sulfate-poor) to determine aerosol pH as follows (Eq. 2):

$$X_T = \frac{m_{\text{Na}^+} + m_{\text{NH}_4^+} + 2m_{\text{Ca}^{2+}}}{m_{\text{SO}_4^{2-}} + m_{\text{HSO}_4^-}}, \quad (2)$$

where m is the concentration of ions in aerosol water in units of mol kg^{-1} .

Under sulfate-rich conditions ($X_T < 2$), the aerosol tends to absorb negligible HNO_3 and HCl due to the high acidity, and sulfate has a pronounced effect on aerosol pH as follows (Eq. 3):

$$m_{\text{H}^+} = 2m_{\text{SO}_4^{2-}} + m_{\text{HSO}_4^-} + m_{\text{NO}_3^-} + m_{\text{Cl}^-} - (2m_{\text{Ca}^{2+}} + m_{\text{NH}_4^+} + m_{\text{Na}^+}) \quad (3a)$$

$$K_{\text{HSO}_4^-} = \left(\frac{m_{\text{H}^+} m_{\text{SO}_4^{2-}}}{m_{\text{HSO}_4^-}} \right) \left(\frac{\gamma_{\text{SO}_4^{2-}} \gamma_{\text{H}^+}}{\gamma_{\text{HSO}_4^-}} \right), \quad (3b)$$

where $K_{\text{HSO}_4^-}$ is the equilibrium constant of the bisulfate ion dissociation in units of $\text{mol}^2 \text{kg}^{-2} \text{atm}^{-1}$, and γ is the activity coefficient of electrolyte calculated by MOSAIC (Zaveri et al., 2005a).

Under sulfate-poor conditions ($X_T > 2$), it is important to account for the gas–aerosol exchange of semi-volatile gases such as HNO_3 , HCl , and NH_3 . Using the internal equilibrium H^+ concentration would lead to oscillations in the condensation and evaporation of these gases, as it does not provide steady-state results (Zaveri et al., 2008). Therefore, MOSAIC employs dynamic H^+ concentrations, which are determined

by the gas–particle exchange of semi-volatile acidic gases (HNO_3 and HCl). And the semi-volatile acidic gases predominantly control aerosol acidic pH as follows (Eq. 4):

$$m_{\text{H}^+} = \frac{K_{\text{HNO}_3}^{\text{gl}} C_{1,\text{HNO}_3}}{\kappa_{\text{HNO}_3} m_{\text{NO}_3^-} (\gamma_{\text{HNO}_3})^2}, \text{ or} \quad (4a)$$

$$m_{\text{H}^+} = \frac{K_{\text{HCl}}^{\text{gl}} C_{1,\text{HCl}}}{\kappa_{\text{HCl}} m_{\text{Cl}^-} (\gamma_{\text{HCl}})^2}, \quad (4b)$$

where m is the concentration of ions in aerosol water, K is the gas–particle equilibrium constant of acidic gases, C_1 is the equilibrium concentrations of acidic matter for the liquid phase in units of mol m^{-3} (air), κ is the first-order mass transfer coefficient, and γ is the activity coefficient of electrolyte calculated by MOSAIC (Zaveri et al., 2008, 2005a, b). Specifically, Eq. (4a) is applied when HNO_3 gas and NO_3 aerosol are both present and have concentrations greater than zero, while Eq. (4b) is used when HCl gas and chloride aerosol concentrations are greater than zero after computing equilibrium surface concentrations. And the aerosol pH is calculated based on H^+ concentrations for each aerosol mode at each time step.

The standard official version of CAM6-Chem does not simulate dust mineralogy or the atmospheric processes of iron solubility change. Instead, it assigns a total iron fraction of 3.5 % to dust, and the dust iron deposition solubility relies on the ratio of coarser dust to fine dust fluxes (Long et al., 2021). In order to properly simulate the diversity of dust iron emissions from different deserts, we developed the model to incorporate five main iron-containing minerals. Each of these minerals includes three distinct dust iron types, thereby providing a more accurate representation of dust mineralogy. We also developed pH-promoted and oxalate-promoted processing in the model to simulate dust iron solubility changes by following the parameterization schemes of Hamilton et al. (2019). More details of model development conducted in this study are described in the next subsection.

2.2 Model development of dust mineralogy and atmospheric processing

In this study, a detailed mineralogy map database (Nickovic et al., 2012) was implemented into the CAM6-Chem model to configure the mineral composition of dust emission. This map is based on the work of Claquin et al. (1999) and has been widely used in previous modeling studies (Johnson and Meskhidze, 2013; Ito and Xu, 2014; Myriokefalitakis et al., 2015). The map segments soil into silt–clay fractions of different minerals, which include five main iron minerals (hematite, smectite, illite, kaolinite, and feldspar). Notably, compared to the mineralogy map from Journet et al. (2014), this mineralogy map has been demonstrated to have a good performance, especially in identifying phyllosilicates with high soluble iron content (Gonçalves Ageitos et al., 2023).

The fractions of five iron minerals in dust aerosols across three modes were determined based on mineral soil distributions (Scanza et al., 2015). Implementing the mineralogy map allows the model to describe dust iron emission from different deserts rather than using a uniform fixed fraction of iron content, which is important for characterizing regional diversity. On top of the mineralogy, we further grouped dust iron into three solubility types – slow soluble (Fe_{ss}), medium soluble (Fe_{ms}), and readily soluble (Fe_{rs}) – with proportions aligned with Hamilton et al. (2019) and Scanza et al. (2018). The detailed iron content and initial iron solubility for each of the five minerals are shown in Table S2. These values are sourced from measurements (Journet et al., 2008; Shi et al., 2011a; Shi et al., 2011b) and are consistent with previous modeling studies (Ito and Xu, 2014; Scanza et al., 2018; Hamilton et al., 2019). Using the mineralogy map, our model achieved simulation of the global spatial patterns of total and initial soluble iron emissions. The total iron content in dust aerosol is higher in the main dust sources, including North Africa, the Middle East, central Asia, and East Asia, and is higher than the default setting of 3.5 % (Fig. S1a). This is consistent with the observations (Lafon et al., 2004, 2006; Shi et al., 2011b) and the research by Ito and Xu (2014), which reported that the observed dust iron content in North Africa and East Asia averaged 3.7 %. Therefore, the use of the mineralogy map increases the iron content in dust from these regions (Fig. S1b), suggesting that the default settings likely underestimate dust iron in these main dust source regions.

We also developed two atmospheric processing of dust iron aerosols via proton-promoted and oxalate-promoted mechanisms in the model. For proton-promoted dissolution, we employ the first-order dissolution rate formula of Lasaga et al. (1994) as follows (Eq. 5) for interstitial iron aerosols:

$$R\text{Fe}_{i,\text{proton}} = K_i(T) \times a(H^+)^{m_i} \times f(\nabla G_r) \times A_i \times \text{MW}_i \quad (5a)$$

$$\frac{d}{dt} [\text{Fe}_{\text{sol, proton}}] = R\text{Fe}_{i,\text{proton}} \times [\text{Fe}_{\text{insol}}], \quad (5b)$$

where $R\text{Fe}_{i,\text{proton}}$ is the proton-promoted iron dissolution rate of which unity is s^{-1} and i represents two types of iron (Fe_{ss} and Fe_{ms}); $K_i(T)$ is the temperature-dependent rate coefficient (Meskhidze et al., 2005); $a(H^+)^{m_i}$ is the proton concentration with an empirical reaction order m_i ; $f(\nabla G_r)$ accounts for the change in the dissolution rate with variation from equilibrium, which equals 1 for simplicity; A is the specific surface area; and MW is the molecular weight. The parameters for the first-order dissolution rate formula (Eq. 5a) are based on previous studies (Meskhidze et al., 2003; Ito and Feng, 2010; Ito and Xu, 2014) and are aligned with Scanza et al. (2018) and Hamilton et al. (2019). For $K_i(T)$ in the Fe_{ms} type, here we use the dissolution rate of mineral illite as an additional simplification following Scanza et al. (2018). In contrast, some studies (Ito and Feng, 2010; Ito, 2012; Ito and Xu, 2014) employ separate dissolution rates

for different minerals. For $K_i(T)$ in the Fe_{ss} type, we use a fast dissolution rate with three stages, following Ito and Xu (2014). The proton-promoted iron dissolution rate is influenced by factors including temperature, dust iron type, and aerosol pH. The simulated aerosol pH in accumulation and coarse mode are shown in Fig. S2. The fine particles are relatively more acidic, while coarse-mode particles are significantly less acidic, influenced by sea salt and dust components. The comparison of annually averaged accumulation-mode aerosols' pH with observations collected by Pye et al. (2020) shows that our model successfully captured the global characteristics of fine aerosol pH. The correlation coefficient and normalized mean bias (NMB) are 0.4 % and 27 % respectively. The discrepancy could be attributed to the seasonal variations and the dynamics of precursor gas emissions, as well as environmental factors such as relative humidity.

For oxalate-promoted dissolution, we employ the first-order dissolution rate formula for cloud-borne iron aerosols as follows (Eq. 6):

$$R\text{Fe}_{i,\text{oxalate}} = a_i \times [\text{C}_2\text{O}_4^{2-}] + b_i \quad (6a)$$

$$\frac{d}{dt} [\text{Fe}_{\text{sol, oxalate}}] = R\text{Fe}_{i,\text{oxalate}} \times [\text{Fe}_{\text{insol}}], \quad (6b)$$

where $R\text{Fe}_{i,\text{oxalate}}$ is the oxalate-promoted iron dissolution rate of which unity is s^{-1} and i represents two types of iron (Fe_{ss} and Fe_{ms}), and the coefficients a_i and b_i are determined by Paris et al. (2011) and aligned with Scanza et al. (2018) and Hamilton et al. (2019). This linear relationship between oxalate-promoted dissolution rate and oxalate concentration in solution is based on cloud water studies by Paris et al. (2011) and has been employed in previous modeling studies (Johnson and Meskhidze, 2013; Myriokefalitakis et al., 2015). Furthermore, Ito and Shi (2016) developed a new oxalate-promoted scheme, which has been applied in recent research (Myriokefalitakis et al., 2022). The default CAM6-Chem model did not include explicit chemistry of oxalate. Therefore, we employ the formula from Hamilton et al. (2019) as follows (Eq. 7) to estimate oxalate concentrations:

$$[\text{C}_2\text{O}_4^{2-}]_{\text{long, lat, lev}} = 150 \times \frac{[\text{SOA}]_{\text{long, lat, lev}}}{\max[\text{SOA}]}, \quad (7)$$

where $[\text{C}_2\text{O}_4^{2-}]_{\text{long, lat, lev}}$ is the estimated oxalate concentration, and $[\text{SOA}]_{\text{long, lat, lev}}$ is the modeled secondary organic aerosol concentration. The formula has been demonstrated to estimate oxalate concentration accurately as both oxalate and SOA are the product of the oxidation of volatile organic carbon gases (Hamilton et al., 2019; Myriokefalitakis et al., 2011). The upper threshold of oxalate concentration is $15 \mu\text{mol L}^{-1}$, keeping consistent with Hamilton et al. (2019) and Scanza et al. (2018). Because the SOA burden simulated in our model version (Fig. S3) is comparable with the previous version (Fig. 5a; Liu et al., 2012). The

maximum SOA concentration was similar to the study of Hamilton et al. (2019). For the oxalate evaluation, we have collected global oxalate observations in rain and cloud water to evaluate our model results. The locations and months are consistent between observations and the model. We utilized monthly mean modeled values, averaged climatologically over the period 2001–2017. Comparisons with observed oxalate levels indicate that our model accurately captures the quantitative characteristics of oxalate, especially in East Asia (Fig. S4). Furthermore, we categorize soluble iron into two types: Fe_{ps}, representing those produced from the proton-promoted processing, and Fe_{os}, representing those produced from the oxalate-promoted processing, enabling an evaluation of these processes' contributions during atmospheric transport.

In this study, simulations of 17 spring seasons from 2001 to 2017 were conducted to analyze long-term spatiotemporal characteristics of dust iron (Table 1). By analyzing the simulation results for the whole year, we found that the spring accounted for 60% of dust deposition and 55% of dust-soluble-iron deposition over the Northwest Pacific of a full year (Fig. S5). Hence, we concentrate our simulation analysis on spring only in this study. For model evaluation purposes, we conducted simulations that aligned with the periods when North Pacific iron observations were available. We also conducted a full-year simulation in 2013, which aligns with the most observations' periods for model evaluation. Two sensitivity experiments were conducted to explore the impact of anthropogenic emissions. All simulations maintained a horizontal resolution of 0.95° by 1.25° (latitude by longitude) and a vertical resolution extending to approximately 40 km with 32 layers (Emmons et al., 2020). Meteorological data from the Modern-Era Retrospective analysis for Research and Applications (MERRA2) reanalysis dataset (Gelaro et al., 2017) were utilized for model adjustment by offline nudging with a relaxation time of 1 h, minimizing meteorological uncertainty. Anthropogenic and biomass burning emissions follow CMIP6 protocols up to 2014 (Eyring et al., 2016), transitioning to the SSP585 scenario thereafter (O'Neill et al., 2017), with emissions over China refined using the MEIC inventory for enhanced local accuracy (Li et al., 2017a; Zheng et al., 2018; Yue et al., 2023).

2.3 Observations

The study employs dust optical depth (DOD) at 550 nm from the MODIS Dust Aerosol (MIDAS) dataset which has a fine resolution of 0.1° × 0.1° and contains daily DOD over 2003–2017 (Gkikas et al., 2021). Hourly PM₁₀ observational data from 1571 sites across China over 2015–2017 spring seasons are sourced from the China National Environmental Monitoring Centre (CNEMC; <http://www.cnemc.cn/>, last access: 22 February 2023). The 230 observational records (~40% are spring) of total and soluble iron concentrations in the North Pacific over 2001–2018 are from the

reported articles (Mahowald et al., 2009; Myriokefalitakis et al., 2018) and GEOTRACES Intermediate Data Product Group (IDP2021v2). Additionally, daily chlorophyll-*a* concentrations are obtained from the OceanColour Climate Change Initiative (OC-CCI, v6.0) products (Sathyendranath et al., 2019).

3 Results and discussion

3.1 Model evaluation

3.1.1 Dust surface concentrations and observed PM₁₀

We first compared simulated dust surface concentrations against observed PM₁₀ levels in East Asia (EA) over 2015–2017 to evaluate model performance in representing dust aerosol mass concentration (Fig. 1). Observed PM₁₀ is a recognized proxy for dust concentrations during high dust event frequencies (Wang et al., 2021; Li et al., 2024). The comparison confirmed a strong concordance between the modeled spatial distribution of dust and observed PM₁₀ values, underscoring the reliability of our model. Dust emitted from the Taklimakan and Gobi deserts was mainly transported eastward and southward, impacting the Northwest Pacific (NWP; 30–50° N, 140° E–160° W). Here we defined the East Asian source region (EAS; 30–50° N, 90–130° E) to represent the origins of dust that may subsequently transport to and deposit over the NWP.

Specifically, evaluation against ground-based measurements suggested a good consistency between simulated dust concentrations and observed PM₁₀ data over the EAS region (Fig. 1b). The average simulated dust surface mass concentration (104 μg m⁻³) closely mirroring the observed PM₁₀ concentration (110 μg m⁻³) over the EAS region. The error margin for the simulated dust concentrations varies between half and twice that of the observed values, indicated by dotted black lines in Fig. 1b. And the normalized mean bias (NMB) is approximately -5.5%. Our model tends to overestimate dust concentrations in the eastern Gobi Desert to some extent. In the North China Plain, the simulated concentrations are slightly lower than the observed PM₁₀ due to high anthropogenic emissions. Overall, these comparisons confirm the proficiency of our model in accurately replicating dust mass concentrations as compared with other related studies (Wang et al., 2021; Liang et al., 2022).

3.1.2 Dust burden and MODIS dust optical depth

The averaged dust burden in the EAS and NWP regions for the spring seasons of 2001–2017 was 2.7 and 0.3 Gg respectively, with the spatial distribution shown in Fig. 2a. Dust particles deposited rapidly, so the burden also gradually decreased from near desert areas to remote ocean during the long-range transport. With respect to the long-term trend, it is well acknowledged that dust over East Asia significantly declined over 2001–2017 (Wu et al., 2022). The MODIS

Table 1. Sensitivity experiments' configurations.

Experiments	Period	Anthropogenic SO ₂ emissions	Anthropogenic NO _x emissions
Base	2001–2017 spring		
Iron evaluation	Align with observations	Updated emissions from MEIC	
pH evaluation	2013		
SO ₂ change	2001 spring	2007 spring	2001 spring
NO _x change	2001 spring	2001 spring	2007 spring

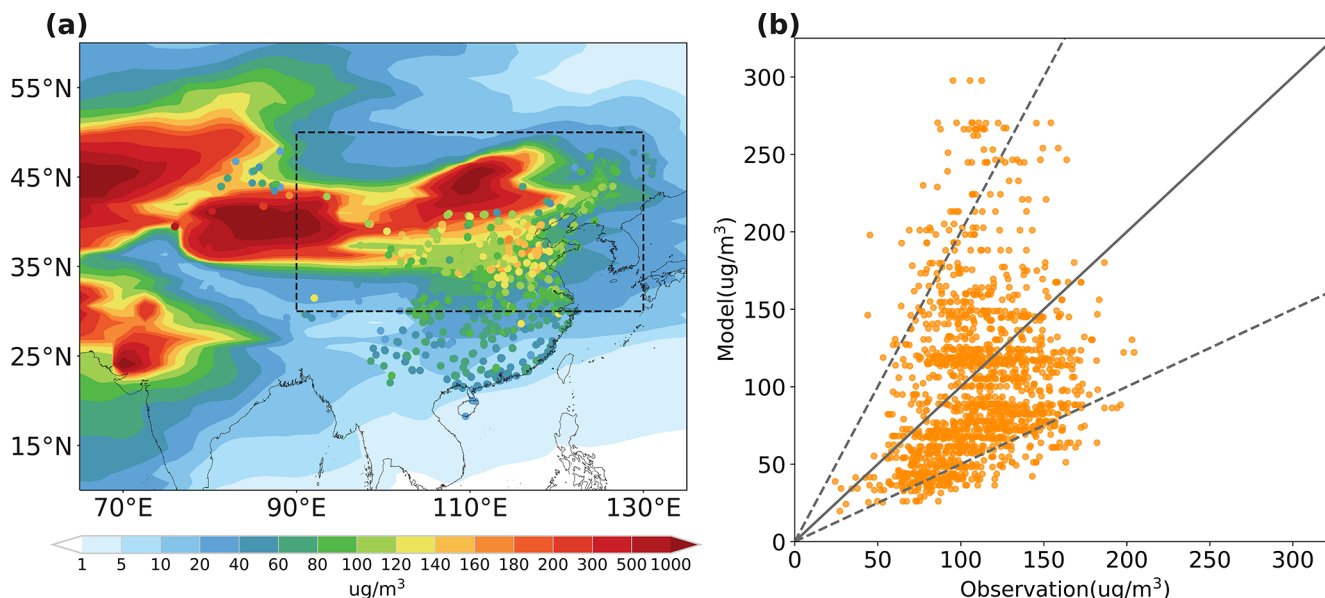


Figure 1. (a) Simulated dust surface mass concentrations and observed PM₁₀ (dots) on average for the 2015–2017 spring seasons. (b) A linear relationship between spring-averaged simulated dust surface mass concentrations and observed PM₁₀ over the East Asian source region (EAS; 30–50° N, 90–130° E) during 2015–2017 spring seasons; the solid black line represents $y = x$, and the dotted black lines represent $y = 0.5/2x$.

DOD product also suggested a decreasing trend by -24% and -27% per decade over EAS and NWP regions respectively, as shown in Fig. 2b and c. Our model results generally agreed well with other studies in reproducing this decreasing trend. The simulated dust burden trend was -3.4% and -8.3% per decade over EAS and NWP regions respectively. Although the interannual variations between the model and MODIS were different for some specific years and our simulation underestimated the magnitude of the declining trend, the model was demonstrated to successfully reproduce the long-term decreased trend of dust over both land and ocean.

3.1.3 Total and soluble iron concentrations

We compared model outputs with observed data for total and soluble iron concentrations over the North Pacific, as shown in Fig. 3. The sampling times and locations of the observed data are presented in Fig. S6. The evaluation ensured temporal and spatial alignment of the simulated data with these ob-

servations. Influenced predominantly by dust activities, both total and soluble iron concentrations are generally higher in spring and lower in winter, as per the observational data. Our model captured these seasonal variations, reinforcing the hypothesis that dust is a major factor influencing iron concentrations in the North Pacific.

The agreement between the model's predictions and ship-based observed data for iron concentrations evidenced our model's ability to simulate iron aerosols. We also compare the performance between the default CAM6-Chem model and our improved model in terms of validation against observations. The developed model achieved a reduction in NMB from -82% to -77% for total iron and from -44% to -33% for soluble iron. For total and soluble iron concentrations, the Pearson correlation coefficients (r) between the simulated results from the developed model and observations are 0.27 and 0.36. Our developed model's evaluations are comparable with other model results (Myriokefalitakis et

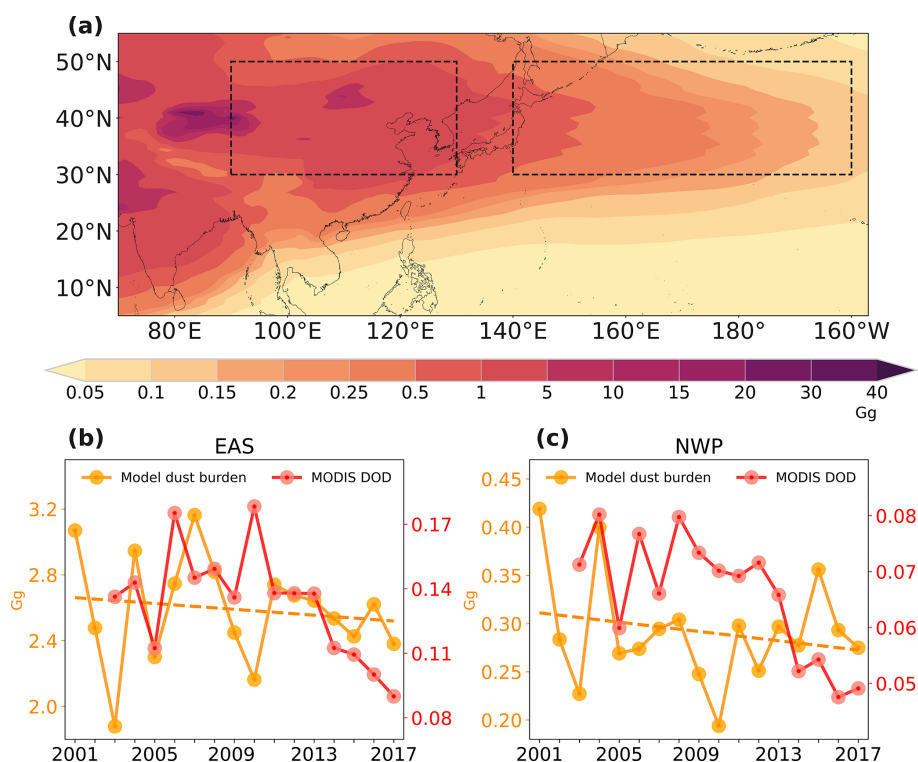


Figure 2. Spatial distributions of simulated dust burden (a) on average for the 2001–2017 spring seasons. Temporal variations of spring-averaged simulated dust burden (yellow line) and MODIS DOD (red line) over (b) East Asian source (EAS; 30–50° N, 90–130° E) and (c) Northwest Pacific (NWP; 30–50° N, 140° E–160° W) regions during 2001–2017 spring seasons.

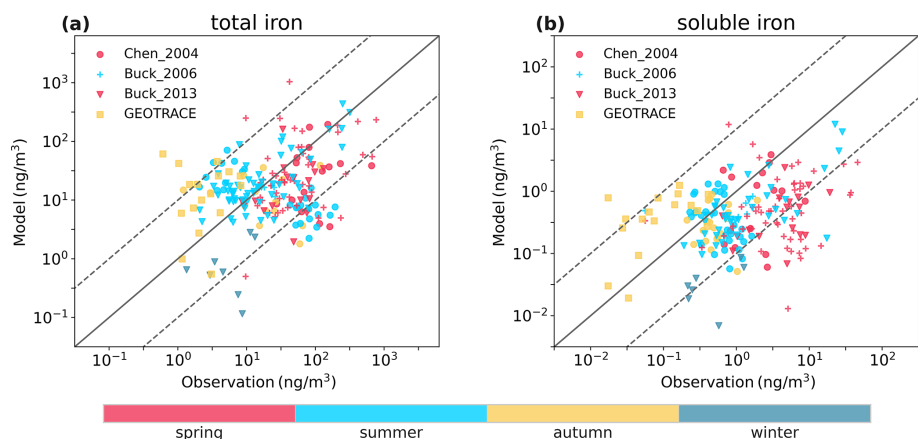


Figure 3. A linear relationship between simulated total (a) and soluble (b) iron concentrations and cruise observations (Chen, 2004; Buck et al., 2006; Buck et al., 2013; GEOTRACES Intermediate Data Product Group, 2021). Different colors and shapes present observations' seasons and cruises respectively.

al., 2022), and this demonstrates our model's good ability to capture the characteristics of total and soluble iron over the North Pacific.

The observations of iron used here are the total iron, which includes dust and pyrogenic iron. The simulated results are lower than observations, likely due to the lack of pyrogenic iron. What is more, the comparison about iron solubility be-

tween simulation and observations is shown in Fig. S7. Our model only calculates iron solubility between 0 % and 10 %. This is likely due to the lack of pyrogenic iron, which has been suggested to contribute to higher iron solubility (Ito et al., 2019).

3.2 Spatial and temporal characteristics of dust iron deposition

3.2.1 Atmospheric dust iron budget

The global mean emissions of dust, dust total iron, and dust-soluble iron were 2707, 109, and 0.98 Tg yr⁻¹, respectively, based on our 2017 model simulation (Table S3). These values are comparable to those reported by the Mechanism of Intermediate complexity for Modelling Iron (MIMI) model (Hamilton et al., 2019) (3200 and 130 Tg yr⁻¹ for dust and dust total iron emissions) but are approximately twice as high as the results from the EC-Earth model (Myriokefalitakis et al., 2022) (1265 and 59.3 Tg yr⁻¹). The simulated global mean iron content in dust is 4.0 %, which aligns well with MIMI (4.1 %) and EC-Earth (4.7 %). The initial iron solubility is 0.91 % and higher than the 0.1 % set by EC-Earth.

The global annual atmospheric dust total and soluble iron budget has been presented in Table 2. The simulated global burdens of dust total and soluble iron were 1331 and 15.4 Gg respectively. The simulated global dust total and soluble iron deposition was 109 and 1.3 Tg yr⁻¹, aligning well with values reported by MIMI (Table 3). Due to higher dust emissions, our simulated dust iron deposition and burdens are nearly double those of the EC-Earth and Ensemble models (Myriokefalitakis et al., 2018). For solubilization rates, the EC-Earth model reported 315 and 170 Gg yr⁻¹ for proton-promoted and oxalate-promoted dissolution, but our results indicated 129 and 200 Gg yr⁻¹. The lower solubilization rate of proton-promoted dissolution and higher solubilization rate of oxalate-promoted dissolution in our study could be attributed to the lower simulated coarse-aerosol-mode acidity and higher scaled oxalate levels than EC-Earth respectively. And the difference in simulation period and iron dissolution mechanisms would also induce discrepancy. For the Northwest Pacific, simulated dust total and soluble iron burdens were 7.4 and 0.11 Gg, aligning closely with Ensemble model results. Dust total and soluble iron deposition rates in this region were 589 and 10.1 Gg yr⁻¹, consistent with both MIMI and Ensemble model estimates. But EC-Earth reported higher NWP deposition rates than our model due to differences in regional dust simulation.

We find through the simulation that dust iron deposition and iron solubility show prominently different spatial distribution patterns (Fig. 4a and c). Dust iron deposition gradually decreased from the source region to the remote ocean, whereas dust iron solubility gradually increased along the transport pathway. In the mainland of EA, simulated dust iron solubility ranged from 0 % to 1.4 %, aligning with observations (Ooki et al., 2009; Shi et al., 2020; Zhang et al., 2023a). Over the downwind oceanic areas, elevated dust iron solubility levels were found, especially in the remote NWP (30–50° N, 160° E–160° W; marked in Fig. 4), which could be up to 2 %. The increasing trend of iron solubility from

land to ocean implied the significant influence of atmospheric processing in altering dust iron during long-range transport.

We further investigated the contributions of proton-promoted and oxalate-promoted processing to soluble iron deposition (Fig. 4b and d). Over the Taklimakan and Gobi deserts, atmospheric processing contributions show little influence on iron solubility due to a lack of acids and oxalate. However, their contributions significantly increased with distance from land along the transport pathway, reaching nearly 40 % over the remote NWP. This underscores the important role of atmospheric processing in dust iron deposition and dust iron solubility, especially over remote ocean areas.

Throughout the spring seasons of 2001–2017, the NWP received an average of 4.9 Gg of soluble iron deposition per season from EA (Fig. 5). The relative contributions of emissions, proton-promoted and oxalate-promoted, to Northwest Pacific dust-soluble-iron deposition in coarse and fine modes are presented in Fig. S8. Atmospheric processing played a significant role (~40 %) in dust-soluble-iron deposition, of which the oxalate-promoted processing emerged as a dominant contributor (25 %). The contribution of the oxalate-promoted processing was about twice that of proton-promoted processing in the NWP. This finding is consistent with global results (Table 2) and aligns with previous global modeling (Johnson and Meskhidze, 2013; Scanza et al., 2018) and East Asian observational research (Shi et al., 2022). Differently, Ito and Shi (2016) and Myriokefalitakis et al. (2022) found that proton-promoted dissolution is the primary process. The higher contribution of oxalate-promoted dissolution in our study might be partially attributed to differences in the parameterization of oxalate concentrations and aerosol acidity between models. The oxalate concentrations appear to be underestimated in their model, and the simulated mainland coarse-mode aerosol acidity in our model (Fig. S2) is obviously lower than those. Furthermore, regional differences can also play a role, as our model performs well for oxalate concentrations over East Asia but not elsewhere (Fig. S4). Future studies should focus on improving these aspects to refine the relative contributions of atmospheric processing. As for different size aerosols' contributions, our modeling results underscore the dominant role of coarse-mode aerosols which accounted for nearly 90 % dust-soluble-iron deposition in the NWP. Fine-mode (Aitken + accumulation) aerosols have a higher iron solubility and could travel a longer distance, but the relatively low mass concentration limited the contribution to iron deposition. And the dominant role of oxalate-promoted processing was mainly determined by the coarse mode (Fig. S8). For the fine mode, proton-promoted processing accounts for approximately 39 % of the soluble iron deposition, which is about 6 times higher than oxalate-promoted processing.

A discernible decline in dust-soluble-iron deposition to the NWP was found over the study period, with an annual reduction rate of approximately 2.4 % yr⁻¹. Dust soluble iron deposition decreased by 31 % from 2001 to 2017 in the spring.

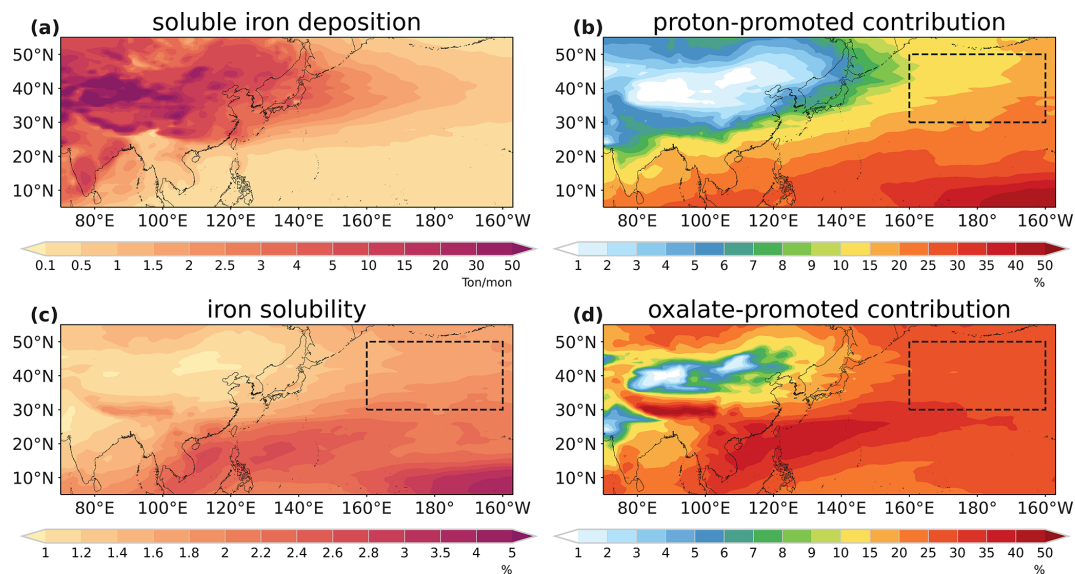


Figure 4. Spatial distributions of (a) soluble iron deposition, (b) proton-promoted relative contributions to soluble iron deposition, (c) iron solubility, and (d) oxalate-promoted contributions to soluble iron deposition on average for the 2001–2017 spring seasons.

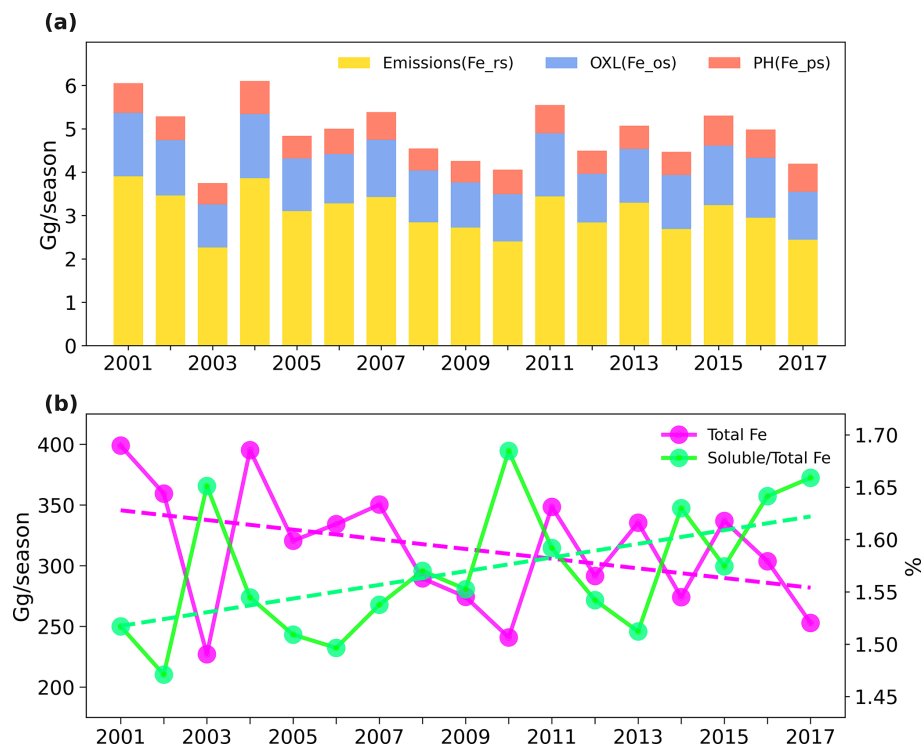


Figure 5. (a) Temporal variations of total soluble iron deposition (stacked bar) and separated soluble iron deposition from emissions (yellow bar), proton-promoted processing (red bar), and oxalate-promoted processing (blue bar) during 2001–2017 spring seasons. (b) Temporal variations of total iron deposition (solid green line) and the ratio of soluble to total iron deposition (solid purple line) during 2001–2017 spring seasons.

Table 2. Global annual atmospheric dust total and soluble iron budget in 2017.

	Burden (Gg)		Dry deposition (Tg yr ⁻¹ and Gg yr ⁻¹)		Wet deposition (Tg yr ⁻¹ and Gg yr ⁻¹)		Solu. rate (Gg yr ⁻¹)	
	Fe_tot	Fe_sol	Fe_tot	Fe_sol	Fe_tot	Fe_sol	Fe_ps	Fe_os
Global	1331	15.4	42.7	445	66.5	874	129	200
coarse, fine	1301, 30	13.3, 2.1	42.2, 0.5	421, 24	65.4, 1.1	789, 85	78, 51	196, 4
NWP	7.4	0.11	0.05	1.2	0.54	8.9	1.3	1.73
coarse, fine	7.1, 0.3	0.09, 0.02	0.05, 0.001	1.1, 0.1	0.53, 0.01	7.8, 1.1	1.1, 0.2	1.68, 0.05

Table 3. Comparison of global annual atmospheric dust total and soluble iron budget from different studies.

		This study		MIMI*		EC-Earth*		Ensemble*	
		Fe_tot	Fe_sol	Fe_tot	Fe_sol	Fe_tot	Fe_sol	Fe_tot	Fe_sol
Global	Burden (Gg)	1331	15.4	/	/	/	6	563	10
	Deposition (Tg yr ⁻¹)	109	1.3	127	1.6	59	0.6	68	0.6
NWP	Burden (Gg)	7.4	0.11	/	/	/	/	5.7	0.18
	Deposition (Gg yr ⁻¹)	589	10.1	472	10.4	2147	33	369	7.7

* The simulation periods are as follows: 2007–2011 for MIMI, 2000–2014 for EC-Earth, and 2007–2014 for the Ensemble.

Among them, both initially emitted and atmospheric processing promoted soluble iron deposition showed a decreasing trend. From 2001 to 2017 in the spring, the deposition of emitted dust-soluble iron, proton-promoted dust-soluble iron, and oxalate-promoted dust-soluble iron over the NWP decreased by 37 %, 5 %, and 24 % respectively. Also, both coarse- and fine-mode soluble iron deposition exhibited a decreasing trend (approximately 30 %).

However, the amount of soluble iron deposition produced from atmospheric processing showed a much lower decrease (18 %) in 2017 compared to the spring of 2001 (Fig. S9). The coarse-mode proton-promoted soluble iron deposition even increased by 7 % as shown in Fig. S9d. This finding indicates that atmospheric processing may offset the decline of dust emission to some extent regarding soluble dust iron deposition over NWP. Figure 5b also suggested that despite the decrease in absolute amounts of dust total and soluble iron deposition (“Total Fe”), the proportion of soluble iron in total dust iron was found to increase over the study period (“soluble/Total Fe”). The proportion increased from 1.5 % in 2001 to 1.7 % in 2017. This increase has contributed an additional 0.4 Gg soluble iron per season to the NWP in 2017 (8 % of the average values). We further probed into the ratios of soluble iron produced by proton-promoted and oxalate-promoted processes in total dust iron and found they both increased prominently (Fig. S10). The increased coarse-mode proton-promoted ratio and oxalate-promoted ratio induced the increase in iron solubility (Fig. S10). Our results suggested that atmospheric processing contributed to the increase in dust iron solubility and mitigated the overall decline trend

in dust-soluble-iron deposition, indicating key factors such as aerosol acidity and in-cloud oxalate.

3.3 Contributions from different driving factors to change of dust iron

To reveal the underlying drivers behind the long-term trend of soluble dust iron deposition, in this section we investigated the changes in dust emission, aerosol pH, and in-cloud oxalate concentrations, while the further contributions of anthropogenic SO₂ and NO_x emissions were quantified through sensitivity simulations.

3.3.1 Dust emissions and surface wind

We first examined the decreasing trend of dust aerosol concentration over EA and found a strong correlation between surface wind speed and dust emission. The Gobi (38–50° N, 100–120° E) and Taklamakan (35–43° N, 80–100° E) deserts are primary sources of dust emissions in EA. Our simulation revealed that the average dust emission flux was 2.3 and 6.5 Gg d⁻¹ in spring over Gobi and Taklamakan, respectively, and surface wind speed was 4.9 and 4.0 m s⁻¹ respectively (Fig. 6c and d). Notably, the correlation coefficients between dust emission flux and surface wind speeds at the Gobi and Taklamakan were 0.7 and 0.6 respectively, underscoring surface wind speed as a pivotal factor in controlling dust emissions. An evident declining trend in surface wind speeds was observed at both dust sources, leading to reduced dust emissions and burdens. This finding is consistent with previous studies (Guan et al., 2017; Wu et al., 2022; Xu et

al., 2020) that also reported the dominant role of surface wind speed in the dust reduction trend in East Asia. Specifically, Guan et al. (2017) and Xu et al. (2020) focused on dust storm events and emphasized the dominant role of maximum surface wind speed based on observed datasets. Our study provided a direct relationship between dust emissions and surface wind speed. Compared to the modeling study by Wu et al. (2022), which mainly focused on the Gobi Desert, we illustrated the dust surface wind's role over the two dust sources including Gobi and Taklamakan Desert. Moreover, the impact of varying wind directions on dust emission and transport was evident. Chen et al. (2017) reported that dust from Gobi was predominantly driven by westerly winds, exerting a greater influence on downwind eastern inland areas and the North Pacific. This relationship was corroborated by our results, which presented more pronounced similarities in the variations of dust deposition to the NWP with dust emissions from the Gobi source compared to the Taklamakan source.

Influenced by the decreased surface wind and dust emissions over two dust sources, dust deposition to the NWP showed a prominent decreasing trend of approximately $2\% \text{ yr}^{-1}$ (yellow line in Fig. 6b). This decrease in dust deposition has induced the decline in dust-soluble-iron deposition (green line in Fig. 6b). The temporal variations in dust-soluble-iron deposition were governed by the variations of dust deposition of which the correlation coefficient was up to 0.96. In conclusion, our findings highlight that the decrease in soluble iron depositions to the NWP can be attributed to the diminished dust emissions, which was induced by declined surface wind speeds over dust sources.

3.3.2 Aerosol pH and anthropogenic emissions

We found an increasing trend in the solubility of dust iron despite the declines in both total and soluble dust iron depositions in the NWP, indicating the effects of atmospheric processing may also change over the study period. So, this section probes into the trend of atmospheric processing and the related variables.

We first explored the proton-promoted processing, where aerosol pH is a key factor influencing soluble iron production. The spatial distribution of surface dust-soluble-iron production rate from proton-promoted processing is shown in Fig. 7a. We find through model simulation that the soluble iron production rate from atmospheric processing primarily peaked at the surface layer of the model (Fig. S11). The most significant production was found over downwind areas of the North China Plain over the Bohai Sea and the Huanghai Sea (shown in dashed rectangles in Fig. 7), which are referred to as high-production areas hereafter. The production of proton-promoted soluble iron is mainly determined by aerosol pH and dust total iron concentrations (Eq. 5). Hence, high-production-rate area was characterized by both relatively high dust concentrations and elevated aerosol acid-

ity (Fig. 7b and d). We analyzed the aerosol pH trend over the high-production area of the proton-promoted processing, which would have a major influence on soluble iron deposition over the NWP (Fig. 7c and e). We found in the simulation that pH values showed different trends in coarse- and fine-mode aerosols. For coarse mode, the averaged pH values in this area demonstrated a noticeable decreasing trend, indicating an enhanced intensity of proton-promoted soluble iron over the study period. For accumulation-mode aerosol, however, the pH value showed a minor increasing trend (Fig. 7e).

To understand the different trends in coarse and fine aerosol pH, we further investigated the key factors (such as acidic gases and CaCO_3) affecting aerosol pH through the MOSAIC mechanism. In the dust source area, CaCO_3 dominated both coarse and accumulation modes of dust. Compared to coarse mode, the content of dust would be relatively lower in accumulation mode, while the content of sulfate, nitrate, and hydrochloride aerosols would be higher. As for coarse-mode pH, it was mostly weakly alkaline according to Eq. (1) ($\text{pH} > 7$ when $T < 25^\circ$) during spring over land areas in EA (Fig. S12a) due to sufficient CaCO_3 content (Fig. 7b). The simulated quasi-neutral pH of continental coarse-mode aerosols has been confirmed by thermodynamic models using aerosol samples, as reported by Fang et al. (2017) and Ding et al. (2019). During the transportation, the solid CaCO_3 would be consumed by acidic gases (H_2SO_4 , HNO_3 , and HCl), which would produce CaSO_4 , $\text{Ca}(\text{NO}_3)_2$, and CaCl_2 (Fig. S12). And coarse-mode aerosol pH became more acidic in the coastal and ocean areas. The acidic pH of oceanic coarse-mode aerosols, which ranged from 2–5, agreed with the estimated results from mineral dust particles (Meskhidze et al., 2003). We find through model simulation that in the coarse mode, H_2SO_4 was almost depleted to produce insoluble CaSO_4 , a condition termed sulfate-poor (Eq. 2, $X_T > 2$). Therefore, in areas of high proton-promoted production, coarse-mode aerosol pH was determined by semi-volatile acidic gases (HNO_3 and HCl), following Eq. (4). As for accumulation-mode aerosol pH, it exhibited higher acidity due to relatively lower CaCO_3 content (Fig. 7d). We find through model simulation that in accumulation mode, sufficient sulfate content resulted in sulfate-rich condition (Eq. 2, $X_T < 2$). Therefore, the emissions of SO_2 have a more pronounced effect on accumulation-mode aerosols' pH following Eq. (3), while it has a very limited impact on coarse-mode aerosols' pH.

Increased coarse aerosol acidity could be attributed to enhanced NO_x and HCl concentrations (Fig. S13) according to the abovementioned functions within the MOSAIC mechanism. Anthropogenic NO_x emission in China increased significantly over 2001–2014, and previous studies also reported the subsequent enhancement of HNO_3 , especially over the North China Plain, with intensive NO_x emission (Luo et al., 2020b). And the increasing trend in HCl concentration was induced by the enhanced HNO_3 gas which would produce HCl gases through heterogeneous reactions

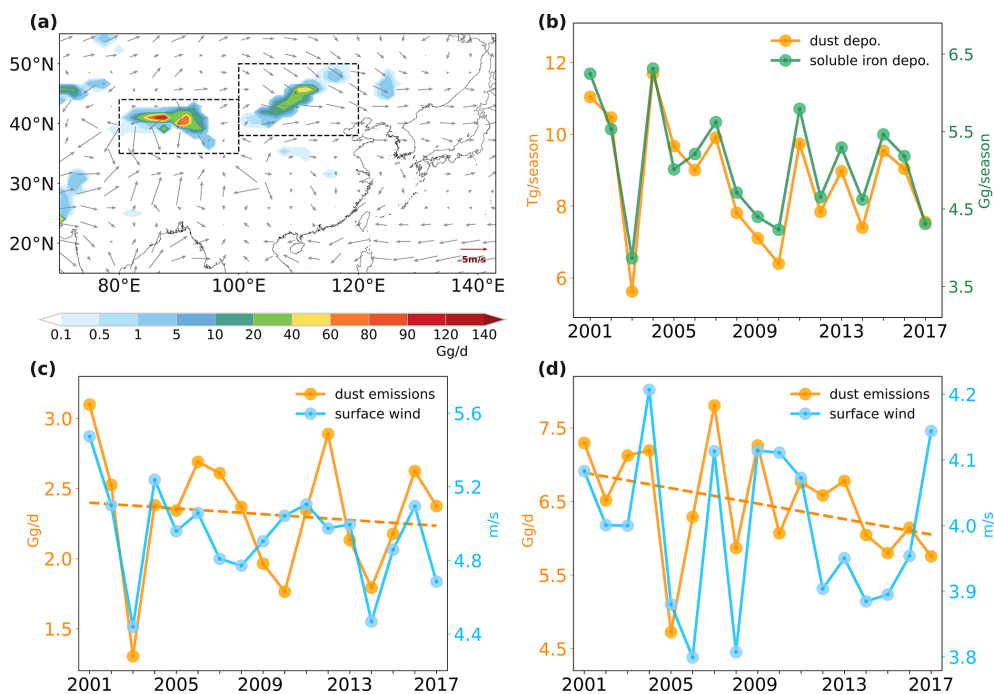


Figure 6. (a) Spatial distributions of dust emission flux and surface wind over East Asia during 2001–2017 spring seasons. (b) Temporal variations of dust (yellow) and soluble iron (green) deposition to the Northwest Pacific (30–50° N, 140° E–160° W). (c, d) Temporal variations of dust emission flux (yellow) and surface wind (blue) over the Gobi dust source (38–50° N, 100–120° E) and Taklamakan dust source (35–43° N, 80–100° E) on average for 2001–2017 spring seasons.

with NaCl/CaCl₂. The increased trend has also been observed along the coast of East Asia (Gromov et al., 2016). Furthermore, decreased dust emissions would also enhance the aerosol acidity due to the lower consumption of acidic gases by CaCO₃ as reported by Karydis et al. (2021). As for accumulation mode, the reduction in anthropogenic SO₂ emissions was expected to decrease aerosol acidity, whereas the reduction in dust emissions could conceivably lead to an increase in aerosol acidity. Within this mechanism, the accumulation-mode pH showed a very minor decreasing trend. Our findings are in agreement with observational studies, highlighting the roles of SO₄²⁻ and non-volatile cations (Ca²⁺) in determining fine particle acidity, which only presented minor changes in EA recently (Ding et al., 2019; Zhou et al., 2022).

Anthropogenic SO₂ emission is usually believed to play an important role in determining aerosol pH and driving the proton-promoted solubility, as reported in previous studies (Li et al., 2017b; Fan et al., 2006), but our simulation results indicated a dominant role by NO_x, which drives the long-term trend of dust iron solubility change. To further consolidate this, two sensitivity experiments were conducted (as illustrated in Table 1) to demonstrate that anthropogenic NO_x emission indeed has a more significant influence on proton-promoted soluble iron deposition than SO₂. We used a higher SO₂ emission for the simulation scenario “SO₂ change” to estimate the impact of SO₂ emission change on soluble iron

by comparing it with baseline simulation and similarly for the scenario “NO_x change”. Compared to the baseline simulation of 2001, concentrations of both SO₂ and NO_x all increased by about 2 ppb averaged in the east and central part of China (the square dashed area outlined in Fig. 8a and d). However, the increase in SO₂ did not induce obvious changes in coarse-mode aerosol pH, while the increase in NO_x notably decreased coarse-mode aerosol pH, especially over coastal areas. In the proton-promoted high-production area (dash outlined in Fig. 8c and f), coarse-mode aerosol pH changed by −0.03 and −0.2, while accumulation-mode aerosol pH changed by −0.2 and +0.02, induced by enhanced SO₂ and NO_x respectively. The decreased fine-mode aerosol acidity over the mainland of EA could be attributed to the increased aerosol water content induced by enhanced NO_x (Fig. S14). As a result, the soluble iron deposition to the NWP increased by 0.01 and 0.03 Gg per season induced by SO₂ and NO_x respectively. Compared with SO₂ emission, which mainly affects accumulation mode, NO_x has a greater impact on proton-promoted soluble iron by affecting coarse mode which dominated (as shown in Sect. 3.2). Our findings underscored the significant impact of anthropogenic NO_x over SO₂ on dust-soluble-iron deposition historically. This result is consistent with the study by Ito and Xu (2014), which showed that future (in 2100) reductions in NO_x which were based on the RCP4.5 would lead to a decrease in soluble iron deposition over the North Pacific (40–60° N, 140–

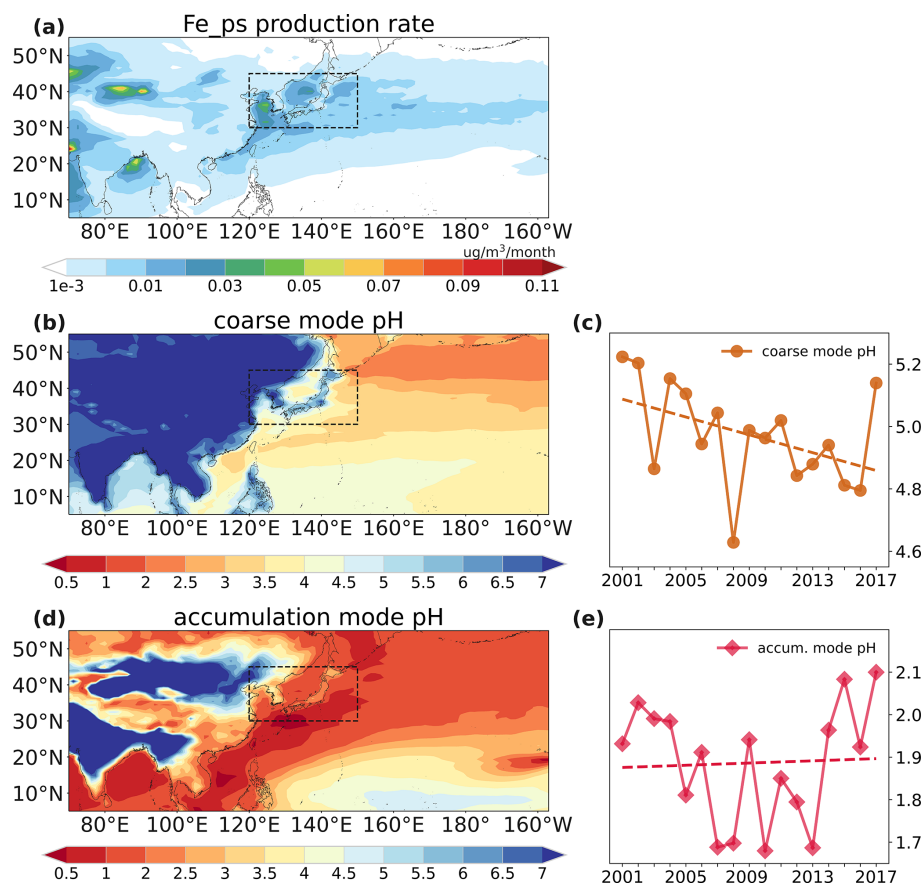


Figure 7. Spatial distributions of surface dust-soluble-iron production rate from proton-promoted processing (a), surface coarse-mode aerosol pH (b), and surface accumulation-mode aerosol pH (d) averaged over the 2001–2017 spring seasons. Temporal variations of surface coarse-mode pH (c) and accumulation-mode pH (e) over high-production-rate area (30–45° N, 120–150° E) averaged over the 2001–2017 spring seasons.

230° E). However, our model also indicated that changes in SO₂ emissions would also contribute to dust-soluble iron deposition changes (approximately one-third of the impact of NO_x). Their model showed that SO₂ had a negligible effect.

In summary, the increase in iron solubility could be attributed to the enhanced acidity of coarse-mode aerosols, driven by anthropogenic NO_x emission change. The interplay of increased NO_x/HCl concentrations and reduced dust emissions has led to an upward trend in coarse-mode aerosol acidity. Conversely, the reduction in SO₂ and dust emissions has counterbalanced their respective effects on fine-mode aerosol acidity, which showed insignificant trends. Our findings suggest that mitigating acidic gas emissions, particularly NO_x, could decelerate dust iron dissolution by influencing aerosol acidity. Furthermore, the reduction in dust emissions would increase aerosol acidity and the induced soluble iron production. Such proton-promoted processing would mitigate the decreasing trend of soluble deposition induced by decreased initial emissions.

3.3.3 Oxalate and cloud environment

We further analyze the key factors (oxalate concentration and cloud fraction) of oxalate-promoted processing. Oxalate concentration has an important effect on the oxalate-promoted soluble iron production according to Eq. (6). In addition, the oxalate-promoted processing only takes place when iron aerosols are in the cloud-borne phase in our model. It has been observed the enhanced iron dissolution when complexation with aerosols occurs in moderately acidic conditions, such as the cloud environment (Cornell and Schindler, 1987; Paris et al., 2011; Xu and Gao, 2008). This setting is consistent with previous studies (Scanza et al., 2018; Hamilton et al., 2019), which were based on the experiment study of Paris et al. (2011). Specifically, the cloud environment represents a cloud fraction higher than 1×10^{-5} and cloud liquid water content (LWC) that is higher than 1×10^{-8} (L/L(cloud)) in the model. The possibility of oxalate-promoted processing would increase if the cloud fraction and LWC increase. Hence, we focus our analysis on two factors, including oxalate concentration and cloud fraction, which is a proxy of

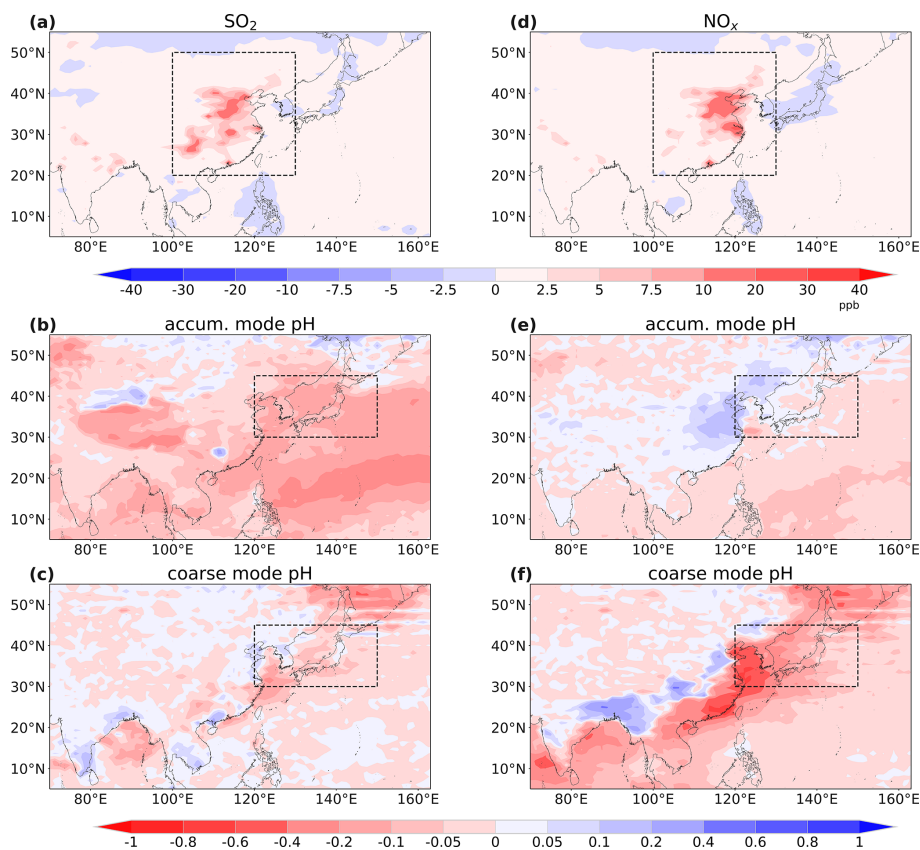


Figure 8. Spatial distributions of surface concentration changes of SO₂ (a) and NO_x (d) in sensitivity experiments and the induced coarse-mode aerosol pH (b and e) and accumulation-mode aerosol pH (c and f) variations respectively.

cloud environment in this section. The spatial distributions of oxalate concentration and cloud fraction are shown in Fig. 9b and d respectively. The spatial pattern of the simulated surface oxalate concentration pattern aligned with the other simulations and in-cloud observations over EA (Myriokefalitakis et al., 2022; Zhao et al., 2019).

As shown in Fig. 9a, the high-production rate of oxalate-promoted processing also peaks in the same area (30–45°N, 120–150°E) as the proton-promoted processing. Both surface oxalate concentrations (Fig. 9b) and cloud fractions (Fig. 9d) were relatively higher in this area, which contributed to the high production of oxalate-promoted processing. The averaged oxalate concentration in the high-production-rate area did not show an obvious increasing trend (Fig. 9c). This finding was consistent with the long-term observations, which presented a tiny increasing trend of oxalate over the western North Pacific (Boreddy et al., 2017). This indicated that oxalate concentration did not drive the change of oxalate-promoted dust iron. We found in the simulation that the surface cloud fraction in the high-production-rate area was enhanced prominently, as shown in Fig. 9e. And the increase in cloud fraction over EA has also been reported by previous studies utilizing ground-based and satellite observations (Huang et al., 2020; Yang et al., 2023). Clouds

are influenced by numerous intricate cloud-controlling factors, such as relative humidity, surface temperature, and estimated inversion strength (Kawai and Shige, 2020; Klein et al., 2017). The increase in surface cloud fraction in the high-production-rate area may be related to the increase in relative humidity (Fig. S15), which plays a significant role in the study of long-term clouds variation (Cao et al., 2021; Yang et al., 2023). Similarly, the temporal LWC was also increased, as shown in Fig. S16. The increased cloud fractions and LWC would provide more possibility for oxalate-promoted processing as it only occurs in the cloud-borne phase, thereby enhancing oxalate-promoted soluble iron production.

3.4 Chlorophyll-*a* response

Our study also integrated simulated soluble iron deposition with satellite chlorophyll-*a* observations to investigate the chlorophyll-*a* response to soluble iron deposition. We found a positive correlation between elevated soluble iron deposition and increased chlorophyll-*a* levels in NWP over the study period. We calculated the relative change in chlorophyll-*a* levels based on the 4 d period preceding and following each soluble iron deposition event. This analysis method was proposed by Westberry et al. (2023) and was

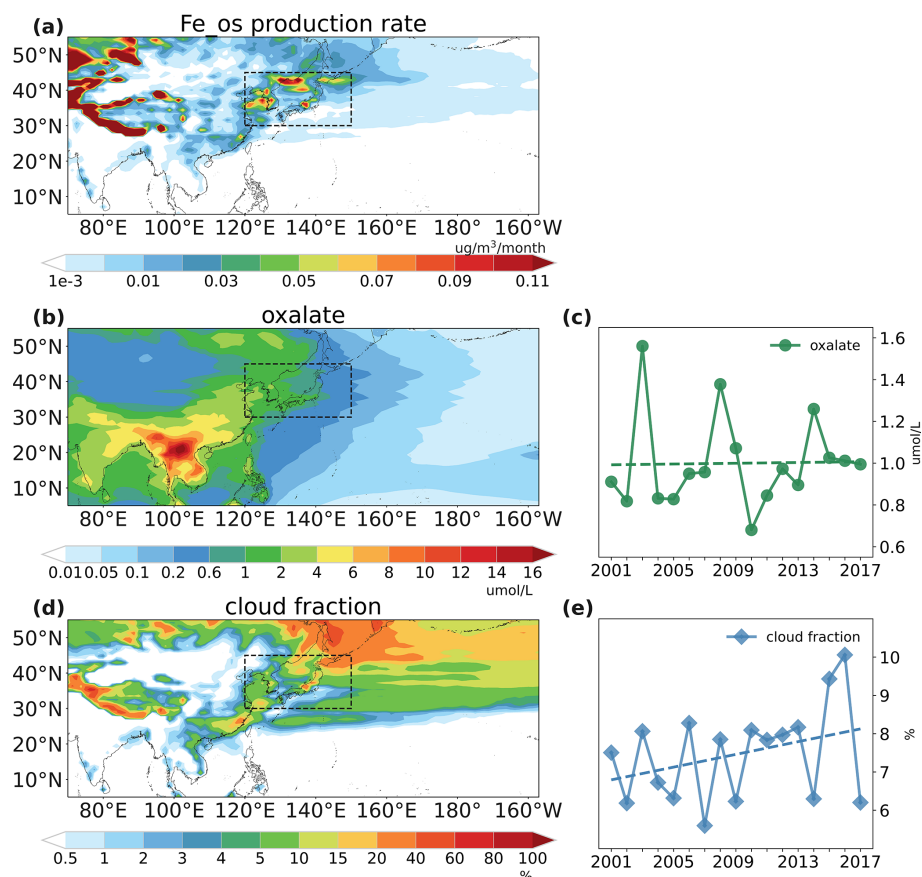


Figure 9. Spatial distributions of surface dust-soluble-iron production rate from oxalate-promoted processing (a), surface oxalate concentrations (b), and surface cloud fractions (d) averaged over the 2001–2017 spring seasons. Temporal variations of surface oxalate concentrations (c) and cloud fractions (e) over high-production-rate area (30–45°N, 120–150°E) averaged over the 2001–2017 spring seasons.

demonstrated to successfully characterize the relationship between iron deposition and chlorophyll-*a* response. This 4 d interval balances the episodic nature of dust events and the typical response time of phytoplankton, which is generally less than 1 week. We identified the highest soluble iron deposition events (HDEs) on an interannual scale for each grid point each spring. The remaining daily data from the 16-year period were categorized as low-deposition events (LDEs). We found in the simulation that soluble iron deposition during HDEs is nearly 8 times that of LDEs in the NWP (Fig. 10a and b).

The probability distribution function of chlorophyll-*a* relative changes after HDEs and LDEs over the NWP region is used to further illustrate the influence of dust iron deposition, as shown in Fig. 10c. Given the typical spring bloom of phytoplankton, the calculated relative responses were predominantly positive. Post-HDE responses showed a more pronounced shift towards positive values compared to LDEs. HDEs resulted in an increased probability of chlorophyll-*a* growth (72 % compared to 61 % for LDEs). Furthermore, the average relative change in chlorophyll-*a* following HDEs was greater than that following LDEs (12 % vs. 9 %). This

probability distribution pattern implied that stronger soluble dust iron inputs can enhance phytoplankton growth over NWP. Previous studies also reported an increase in phytoplankton growth after intensive dust deposition in the NWP (Zhang et al., 2023b; Luo et al., 2020a; Yoon et al., 2017). However, it is important to notice that phytoplankton dynamics are also influenced by various other factors, including sea surface temperature, mixed layer depth, and upwelling transport. To isolate the impact of dust-soluble iron on phytoplankton, more targeted experiments and simulations are required, such as applying a fully coupled Earth system model.

4 Conclusions and summary

This study employs an advanced modeling approach to provide a long-term analysis of the spatiotemporal dynamics and driving factors influencing dust-soluble-iron deposition in the Northwest Pacific in the spring of 2001–2017. We performed simulations of dust total and soluble iron emissions, transport, and deposition with the CAM6-Chem model. The developed model incorporated a mineralogy map of dust iron emissions and accounted for two primary atmospheric

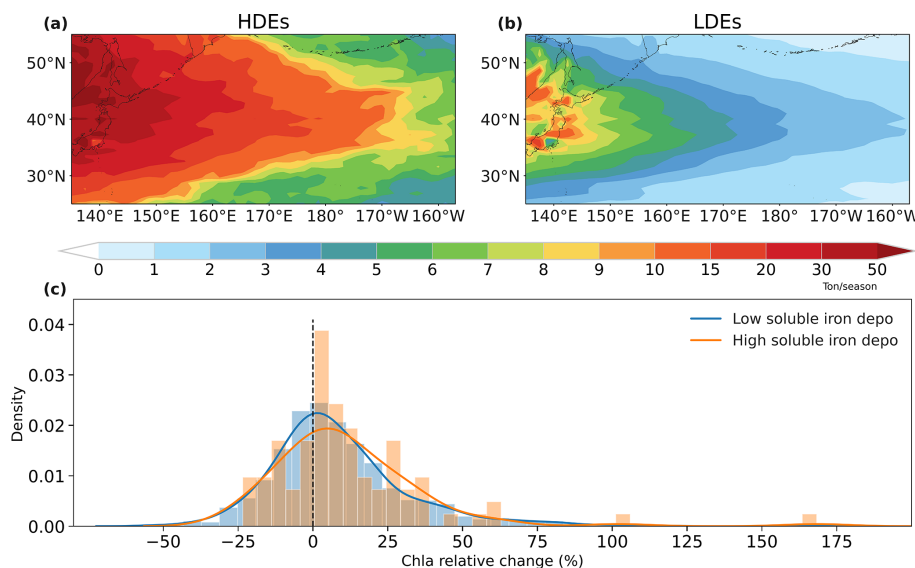


Figure 10. Spatial distributions of selected high (a) and low (b) soluble iron deposition averaged over the 2001–2017 spring seasons. (c) Probability distribution function of relative changes in chlorophyll-*a* averaged over NWP after high (orange) and low (blue) deposition events.

processing – proton-promoted and oxalate-promoted mechanisms – that induce iron dissolution. Validated against multiple observational datasets, our model successfully captured the characteristics of total and soluble iron over the North Pacific.

We found through the simulation that the average deposition of dust-soluble iron to the Northwest Pacific was 4.9 Gg per season. Atmospheric processing played a significant role ($\sim 40\%$) in dust-soluble-iron deposition of which the oxalate-promoted processing emerged as a dominant contributor (25%). A decline in surface wind strength over dust source regions in East Asia led to a 2.4% annual decrease in dust-soluble-iron deposition. However, the proportion of dust-soluble iron within the total deposition has been rising, despite the general decrease in both total and soluble iron deposition. This increase has contributed an additional 0.4 Gg soluble iron per season to the NWP in 2017 (8% of the average values). On the one hand, the increase in iron solubility can be attributed to enhanced NO_x/HCl emissions and reduced dust emissions, which increased coarse-mode aerosol acidity and iron dissolution. On the other hand, the increased surface cloud fractions accelerated the oxalate-promoted processing and induced more dust-soluble-iron production. Atmospheric processing has thus been identified as a crucial factor in promoting soluble iron production and deposition in the Northwest Pacific. Furthermore, our findings indicate that anthropogenic NO_x emissions exert a more significant influence on the dissolution of dust-soluble iron through proton-promoted processing rather than SO_2 . As for the marine ecology of dust-soluble-iron deposition, our study establishes a link between high dust-soluble iron depositions and increased chlorophyll-*a* levels in the NWP. It highlights

the ecological significance of soluble iron inputs in promoting phytoplankton growth and the potential ecology effect induced by declined dust-soluble-iron deposition in the Northwest Pacific.

It is crucial to acknowledge that this study focuses on spring dust sources of iron, but pyrogenic iron sources, such as those from anthropogenic activities and biomass burning in other seasons, also make a substantial contribution to the ocean's soluble iron inventory due to their high solubility (Ito et al., 2021, 2019; Rathod et al., 2020). The increased anthropogenic soluble iron deposition trend during our study period could oppose the decreased dust-soluble-iron deposition to some extent (Hamilton et al., 2020). Future studies should include these additional iron sources to provide a more comprehensive assessment of soluble iron and its ecological impacts throughout the year. Additionally, further investigation into other atmospheric processing that facilitates iron dissolution, such as irradiation effects (Faust and Hoigné, 1990; Spokes and Jickells, 1995) and the influence of various organic matter ligands (Chen and Grassian, 2013; Sakata et al., 2022), is necessary. The lack of an explicit chemical simulation for oxalate in our study highlights the need for continued development in understanding iron dissolution mechanisms, aiming to improve the model's ability to simulate soluble iron in dust accurately. Given the limitations of the Community Earth System Model (CESM2) in simulating dust dynamics (Wu et al., 2020), urgent advancements are needed in modeling dust emissions, transport, and deposition processes to enhance the accuracy of dust iron simulations (Li et al., 2022; Leung et al., 2023).

In summary, our research delineates a quantitative decrease in dust bioavailable iron deposition in the Northwest

Pacific, which may have broader ecological consequences. We emphasize the importance of atmospheric processing including the proton-promoted and oxalate-promoted mechanisms in the dissolution of dust iron. Initial emissions of both land and atmospheric processing play an important role in dust bioavailable iron deposition and the subsequent marine ecology effect. Amidst the evolving global environmental challenges, a holistic understanding of the complex interactions in the Earth system and the impact of human activities is essential.

Code and data availability. The code and data of our developed model are available on request.

Supplement. The supplement related to this article is available online at <https://doi.org/10.5194/acp-25-5175-2025-supplement>.

Author contributions. HZ: conceptualization, formal analysis, investigation, methodology, visualization, writing (original draft), writing (review and editing). YL: methodology. MY: methodology. SF: formal analysis, writing (review and editing). PF: formal analysis, writing (review and editing). KH: formal analysis, writing (review and editing). XD: conceptualization, formal analysis, investigation, project administration, supervision, writing (original draft), writing (review and editing). MW: project administration, supervision, writing (review and editing).

Competing interests. At least one of the (co-)authors is a member of the editorial board of *Atmospheric Chemistry and Physics*. The peer-review process was guided by an independent editor, and the authors also have no other competing interests to declare.

Disclaimer. Publisher's note: Copernicus Publications remains neutral with regard to jurisdictional claims made in the text, published maps, institutional affiliations, or any other geographical representation in this paper. While Copernicus Publications makes every effort to include appropriate place names, the final responsibility lies with the authors.

Special issue statement. This article is part of the special issue "RUSTED: Reducing Uncertainty in Soluble aerosol Trace Element Deposition (AMT/ACP/AR/BG inter-journal SI)". It is not associated with a conference.

Acknowledgements. This work acknowledges the financial support from the National Natural Science Foundation of China (grant nos. 42361144711 and U2342223) and the Fundamental Research Funds for the Central Universities – CEMAC "GeoX" Interdisciplinary Program (2024ZD05) by the Frontiers Science Center for Critical Earth Material Cycling, Nanjing University, as well as

the Collaborative Innovation Center of Climate Change, Jiangsu Province. We also appreciate the High Performance Computing Center of Nanjing University for providing the computational resources essential for this research. Special thanks are extended to all the scientists, software engineers, and administrators involved in the development of the CESM2 model. We acknowledge the observation data from GEOTRACES. The GEOTRACES 2021 Intermediate Data Product version 2 (IDP2021v2) represents an international collaboration and is endorsed by the Scientific Committee on Oceanic Research (SCOR). The many researchers and funding agencies responsible for the collection of data and quality control are thanked for their contributions to the IDP2021v2. Additionally, we are grateful to the anonymous reviewers for their valuable feedback and suggestions aimed at enhancing the quality of the paper.

Financial support. This research has been supported by the National Natural Science Foundation of China (grant nos. 42361144711 and U2342223) and the Fundamental Research Funds for the Central Universities (grant no. 2024ZD05).

Review statement. This paper was edited by Maria Kanakidou and reviewed by Akinori Ito and one anonymous referee.

References

- Bergas-Massó, E., Gonçalves Ageitos, M., Myriokefalitakis, S., Miller, R. L., van Noije, T., Le Sager, P., Montané Pinto, G., and Pérez García-Pando, C.: Pre-Industrial, Present and Future Atmospheric Soluble Iron Deposition and the Role of Aerosol Acidity and Oxalate Under CMIP6 Emissions, *Earth's Future*, 11, e2022EF003353, <https://doi.org/10.1029/2022EF003353>, 2023.
- Boreddy, S. K. R., Kawamura, K., and Tachibana, E.: Long-term (2001–2013) observations of water-soluble dicarboxylic acids and related compounds over the western North Pacific: trends, seasonality and source apportionment, *Scientific Reports*, 7, 8518, <https://doi.org/10.1038/s41598-017-08745-w>, 2017.
- Buck, C. S., Landing, W. M., Resing, J. A., and Lebon, G. T.: Aerosol iron and aluminum solubility in the northwest Pacific Ocean: Results from the 2002 IOC cruise, *Geochem. Geophys. Geosy.*, 7, Q04M07, <https://doi.org/10.1029/2005GC000977>, 2006.
- Buck, C. S., Landing, W. M., and Resing, J.: Pacific Ocean aerosols: Deposition and solubility of iron, aluminum, and other trace elements, *Mar. Chem.*, 157, 117–130, <https://doi.org/10.1016/j.marchem.2013.09.005>, 2013.
- Cao, Y., Wang, M., Rosenfeld, D., Zhu, Y., Liang, Y., Liu, Z., and Bai, H.: Strong Aerosol Effects on Cloud Amount Based on Long-Term Satellite Observations Over the East Coast of the United States, *Geophys. Res. Lett.*, 48, e2020GL091275, <https://doi.org/10.1029/2020GL091275>, 2021.
- Chen, H. and Grassian, V. H.: Iron Dissolution of Dust Source Materials during Simulated Acidic Processing: The Effect of Sulfuric, Acetic, and Oxalic Acids, *Environ. Sci. Technol.*, 47, 10312–10321, <https://doi.org/10.1021/es401285s>, 2013.

- Chen, S., Huang, J., Li, J., Jia, R., Jiang, N., Kang, L., Ma, X., and Xie, T.: Comparison of dust emissions, transport, and deposition between the Taklimakan Desert and Gobi Desert from 2007 to 2011, *Science China Earth Sciences*, 60, 1338–1355, <https://doi.org/10.1007/s11430-016-9051-0>, 2017.
- Chen, Y.: Sources and fate of atmospheric nutrients over the remote oceans and their role on controlling marine diazotrophic microorganisms, Doctoral dissertation, <https://drum.lib.umd.edu/handle/1903/1967> (last access: 13 June 2023), 2004.
- Claquin, T., Schulz, M., and Balkanski, Y. J.: Modeling the mineralogy of atmospheric dust sources, *J. Geophys. Res.-Atmos.*, 104, 22243–22256, <https://doi.org/10.1029/1999JD900416>, 1999.
- Cornell, R. M. and Schindler, P. W.: Photochemical Dissolution of Goethite in Acid/Oxalate Solution, *Clay Clay Miner.*, 35, 347–352, <https://doi.org/10.1346/CCMN.1987.0350504>, 1987.
- Danabasoglu, G., Lamarque, J.-F., Bacmeister, J., Bailey, D. A., DuVivier, A. K., Edwards, J., Emmons, L. K., Fasullo, J., Garcia, R., Gettelman, A., Hannay, C., Holland, M. M., Large, W. G., Lauritzen, P. H., Lawrence, D. M., Lenaerts, J. T. M., Lindsay, K., Lipscomb, W. H., Mills, M. J., Neale, R., Oleson, K. W., Otto-Bliesner, B., Phillips, A. S., Sacks, W., Tilmes, S., van Kampenhout, L., Vertenstein, M., Bertini, A., Dennis, J., Deser, C., Fischer, C., Fox-Kemper, B., Kay, J. E., Kinnison, D., Kushner, P. J., Larson, V. E., Long, M. C., Mickelson, S., Moore, J. K., Nienhouse, E., Polvani, L., Rasch, P. J., and Strand, W. G.: The Community Earth System Model Version 2 (CESM2), *J. Adv. Model. Earth Sy.*, 12, e2019MS001916, <https://doi.org/10.1029/2019MS001916>, 2020.
- Ding, J., Zhao, P., Su, J., Dong, Q., Du, X., and Zhang, Y.: Aerosol pH and its driving factors in Beijing, *Atmos. Chem. Phys.*, 19, 7939–7954, <https://doi.org/10.5194/acp-19-7939-2019>, 2019.
- Emmons, L. K., Schwantes, R. H., Orlando, J. J., Tyndall, G., Kinnison, D., Lamarque, J.-F., Marsh, D., Mills, M. J., Tilmes, S., Bardeen, C., Buchholz, R. R., Conley, A., Gettelman, A., Garcia, R., Simpson, I., Blake, D. R., Meinardi, S., and Pétron, G.: The Chemistry Mechanism in the Community Earth System Model Version 2 (CESM2), *J. Adv. Model. Earth Sy.*, 12, e2019MS001882, <https://doi.org/10.1029/2019MS001882>, 2020.
- Eyring, V., Bony, S., Meehl, G. A., Senior, C. A., Stevens, B., Stouffer, R. J., and Taylor, K. E.: Overview of the Coupled Model Intercomparison Project Phase 6 (CMIP6) experimental design and organization, *Geosci. Model Dev.*, 9, 1937–1958, <https://doi.org/10.5194/gmd-9-1937-2016>, 2016.
- Fan, S.-M., Moxim, W. J., and Levy II, H.: Aeolian input of bioavailable iron to the ocean, *Geophys. Res. Lett.*, 33, L07602, <https://doi.org/10.1029/2005GL024852>, 2006.
- Fang, T., Guo, H., Zeng, L., Verma, V., Nenes, A., and Weber, R. J.: Highly Acidic Ambient Particles, Soluble Metals, and Oxidative Potential: A Link between Sulfate and Aerosol Toxicity, *Environ. Sci. Technol.*, 51, 2611–2620, <https://doi.org/10.1021/acs.est.6b06151>, 2017.
- Faust, B. C. and Hoigné, J.: Photolysis of Fe (III)-hydroxy complexes as sources of OH radicals in clouds, fog and rain, *Atmos. Environ. A-Gen.*, 24, 79–89, [https://doi.org/10.1016/0960-1686\(90\)90443-Q](https://doi.org/10.1016/0960-1686(90)90443-Q), 1990.
- Gelaro, R., McCarty, W., Suárez, M. J., Todling, R., Molod, A., Takacs, L., Randles, C. A., Darmenov, A., Bosilovich, M. G., Reichle, R., Wargan, K., Coy, L., Cullather, R., Draper, C., Akella, S., Buchard, V., Conaty, A., da Silva, A. M., Gu, W., Kim, G.-K., Koster, R., Lucchesi, R., Merkova, D., Nielsen, J. E., Parityka, G., Pawson, S., Putman, W., Rienecker, M., Schubert, S. D., Sienkiewicz, M., and Zhao, B.: The Modern-Era Retrospective Analysis for Research and Applications, Version 2 (MERRA-2), *J. Climate*, 30, 5419–5454, <https://doi.org/10.1175/JCLI-D-16-0758.1>, 2017.
- GEO-TRACES Intermediate Data Product Group: The GEO-TRACES Intermediate Data Product 2021 version 2 (IDP2021v2), NERC EDS British Oceanographic Data Centre NOC [data set], <https://doi.org/10.5285/ff46f034-f47c-05f9-e053-6c86abc0dc7e>, 2021.
- Gkikas, A., Proestakis, E., Amiridis, V., Kazadzis, S., Di Tomaso, E., Tsekeri, A., Marinou, E., Hatzianastassiou, N., and Pérez García-Pando, C.: ModIs Dust AeroSol (MIDAS): a global fine-resolution dust optical depth data set, *Atmos. Meas. Tech.*, 14, 309–334, <https://doi.org/10.5194/amt-14-309-2021>, 2021.
- Gonçalves Ageitos, M., Obiso, V., Miller, R. L., Jorba, O., Klose, M., Dawson, M., Balkanski, Y., Perlwitz, J., Basart, S., Di Tomaso, E., Escribano, J., Macchia, F., Montané, G., Mahowald, N. M., Green, R. O., Thompson, D. R., and Pérez García-Pando, C.: Modeling dust mineralogical composition: sensitivity to soil mineralogy atlases and their expected climate impacts, *Atmos. Chem. Phys.*, 23, 8623–8657, <https://doi.org/10.5194/acp-23-8623-2023>, 2023.
- Gromov, S. A., Trifonova-Yakovleva, A., and Gromov, S. S.: Intraregional links between the trends in air pollutants observed at the EANET network sites for 2000–2014, EGU General Assembly 2016, 18–22 April 2016, EGU2016-17138, <https://meetingorganizer.copernicus.org/EGU2016/EGU2016-17138-1.pdf> (last access: 12 July 2024), 2016.
- Guan, Q., Sun, X., Yang, J., Pan, B., Zhao, S., and Wang, L.: Dust Storms in Northern China: Long-Term Spatiotemporal Characteristics and Climate Controls, *J. Climate*, 30, 6683–6700, <https://doi.org/10.1175/JCLI-D-16-0795.1>, 2017.
- Guo, J., Lou, M., Miao, Y., Wang, Y., Zeng, Z., Liu, H., He, J., Xu, H., Wang, F., Min, M., and Zhai, P.: Trans-Pacific transport of dust aerosols from East Asia: Insights gained from multiple observations and modeling, *Environ. Pollut.*, 230, 1030–1039, <https://doi.org/10.1016/j.envpol.2017.07.062>, 2017.
- Hamilton, D. S., Scanza, R. A., Feng, Y., Guinness, J., Kok, J. F., Li, L., Liu, X., Rathod, S. D., Wan, J. S., Wu, M., and Mahowald, N. M.: Improved methodologies for Earth system modelling of atmospheric soluble iron and observation comparisons using the Mechanism of Intermediate complexity for Modelling Iron (MIMI v1.0), *Geosci. Model Dev.*, 12, 3835–3862, <https://doi.org/10.5194/gmd-12-3835-2019>, 2019.
- Hamilton, D. S., Scanza, R. A., Rathod, S. D., Bond, T. C., Kok, J. F., Li, L., Matsui, H., and Mahowald, N. M.: Recent (1980 to 2015) Trends and Variability in Daily-to-Interannual Soluble Iron Deposition from Dust, Fire, and Anthropogenic Sources, *Geophys. Res. Lett.*, 47, e2020GL089688, <https://doi.org/10.1029/2020GL089688>, 2020.
- Hettiarachchi, E., Ivanov, S., Kieft, T., Goldstein, H. L., Moskowicz, B. M., Reynolds, R. L., and Rubasinghege, G.: Atmospheric Processing of Iron-Bearing Mineral Dust Aerosol and Its Effect on Growth of a Marine Diatom, *Cyclotella meneghiniana*, *Environ. Sci. Technol.*, 55, 871–881, <https://doi.org/10.1021/acs.est.0c06995>, 2021.

- Huang, J., Bu, L., Kumar, K. R., Khan, R., and Devi, N. S. M. P. L.: Investigating the relationship between aerosol and cloud optical properties inferred from the MODIS sensor in recent decades over East China, *Atmos. Environ.*, 239, 117812, <https://doi.org/10.1016/j.atmosenv.2020.117812>, 2020.
- Ito, A.: Contrasting the Effect of Iron Mobilization on Soluble Iron Deposition to the Ocean in the Northern and Southern Hemispheres, *J. Meteorol. Soc. Jpn.*, 90A, 167–188, <https://doi.org/10.2151/jmsj.2012-A09>, 2012.
- Ito, A.: Atmospheric Processing of Combustion Aerosols as a Source of Bioavailable Iron, *Environ. Sci. Tech. Lett.*, 2, 70–75, <https://doi.org/10.1021/acs.estlett.5b00007>, 2015.
- Ito, A. and Feng, Y.: Role of dust alkalinity in acid mobilization of iron, *Atmos. Chem. Phys.*, 10, 9237–9250, <https://doi.org/10.5194/acp-10-9237-2010>, 2010.
- Ito, A. and Shi, Z.: Delivery of anthropogenic bioavailable iron from mineral dust and combustion aerosols to the ocean, *Atmos. Chem. Phys.*, 16, 85–99, <https://doi.org/10.5194/acp-16-85-2016>, 2016.
- Ito, A. and Xu, L.: Response of acid mobilization of iron-containing mineral dust to improvement of air quality projected in the future, *Atmos. Chem. Phys.*, 14, 3441–3459, <https://doi.org/10.5194/acp-14-3441-2014>, 2014.
- Ito, A., Myriokefalitakis, S., Kanakidou, M., Mahowald, N. M., Scanza, R. A., Hamilton, D. S., Baker, A. R., Jickells, T., Sarin, M., Bikkina, S., Gao, Y., Shelley, R. U., Buck, C. S., Landing, W. M., Bowie, A. R., Perron, M. M. G., Guieu, C., Meskhidze, N., Johnson, M. S., Feng, Y., Kok, J. F., Nenes, A., and Duce, R. A.: Pyrogenic iron: The missing link to high iron solubility in aerosols, *Science Advances*, 5, eaau7671, <https://doi.org/10.1126/sciadv.aau7671>, 2019.
- Ito, A., Ye, Y., Baldo, C., and Shi, Z.: Ocean fertilization by pyrogenic aerosol iron, *npj Climate and Atmospheric Science*, 4, 30, <https://doi.org/10.1038/s41612-021-00185-8>, 2021.
- Jickells, T. and Moore, C. M.: The Importance of Atmospheric Deposition for Ocean Productivity, *Annu. Rev. Ecol. Evol. S.*, 46, 481–501, <https://doi.org/10.1146/annurev-ecolsys-112414-054118>, 2015.
- Jickells, T., Boyd, P., and Hunter, K. A.: Biogeochemical Impacts of Dust on the Global Carbon Cycle, in: *Mineral Dust: A Key Player in the Earth System*, edited by: Knippertz, P. and Stuut, J.-B. W., Springer Netherlands, Dordrecht, 359–384, https://doi.org/10.1007/978-94-017-8978-3_14, 2014.
- Jickells, T. D., An, Z. S., Andersen, K. K., Baker, A. R., Bergametti, G., Brooks, N., Cao, J. J., Boyd, P. W., Duce, R. A., Hunter, K. A., Kawahata, H., Kubilay, N., laRoche, J., Liss, P. S., Mahowald, N., Prospero, J. M., Ridgwell, A. J., Tegen, I., and Torres, R.: Global Iron Connections Between Desert Dust, Ocean Biogeochemistry, and Climate, *Science*, 308, 67–71, <https://doi.org/10.1126/science.1105959>, 2005.
- Jo, D. S., Hodzic, A., Emmons, L. K., Marais, E. A., Peng, Z., Nault, B. A., Hu, W., Campuzano-Jost, P., and Jimenez, J. L.: A simplified parameterization of isoprene-epoxydiol-derived secondary organic aerosol (IEPOX-SOA) for global chemistry and climate models: a case study with GEOS-Chem v11-02-rc, *Geosci. Model Dev.*, 12, 2983–3000, <https://doi.org/10.5194/gmd-12-2983-2019>, 2019.
- Jo, D. S., Hodzic, A., Emmons, L. K., Tilmes, S., Schwantes, R. H., Mills, M. J., Campuzano-Jost, P., Hu, W., Zaveri, R. A., Easter, R. C., Singh, B., Lu, Z., Schulz, C., Schneider, J., Shilling, J. E., Wisthaler, A., and Jimenez, J. L.: Future changes in isoprene-epoxydiol-derived secondary organic aerosol (IEPOX SOA) under the Shared Socioeconomic Pathways: the importance of physicochemical dependency, *Atmos. Chem. Phys.*, 21, 3395–3425, <https://doi.org/10.5194/acp-21-3395-2021>, 2021.
- Johnson, M. S. and Meskhidze, N.: Atmospheric dissolved iron deposition to the global oceans: effects of oxalate-promoted Fe dissolution, photochemical redox cycling, and dust mineralogy, *Geosci. Model Dev.*, 6, 1137–1155, <https://doi.org/10.5194/gmd-6-1137-2013>, 2013.
- Journet, E., Desboeufs, K. V., Caquineau, S., and Colin, J.-L.: Mineralogy as a critical factor of dust iron solubility, *Geophys. Res. Lett.*, 35, L07805, <https://doi.org/10.1029/2007GL031589>, 2008.
- Journet, E., Balkanski, Y., and Harrison, S. P.: A new data set of soil mineralogy for dust-cycle modeling, *Atmos. Chem. Phys.*, 14, 3801–3816, <https://doi.org/10.5194/acp-14-3801-2014>, 2014.
- Karydis, V. A., Tsimpidi, A. P., Bacer, S., Pozzer, A., Nenes, A., and Lelieveld, J.: Global impact of mineral dust on cloud droplet number concentration, *Atmos. Chem. Phys.*, 17, 5601–5621, <https://doi.org/10.5194/acp-17-5601-2017>, 2017.
- Karydis, V. A., Tsimpidi, A. P., Pozzer, A., and Lelieveld, J.: How alkaline compounds control atmospheric aerosol particle acidity, *Atmos. Chem. Phys.*, 21, 14983–15001, <https://doi.org/10.5194/acp-21-14983-2021>, 2021.
- Kawai, H. and Shige, S.: Marine Low Clouds and their Parameterization in Climate Models, *J. Meteorol. Soc. Jpn. Ser. II*, 98, 1097–1127, <https://doi.org/10.2151/jmsj.2020-059>, 2020.
- Klein, S. A., Hall, A., Norris, J. R., and Pincus, R.: Low-Cloud Feedbacks from Cloud-Controlling Factors: A Review, *Surv. Geophys.*, 38, 1307–1329, <https://doi.org/10.1007/s10712-017-9433-3>, 2017.
- Kok, J. F.: A scaling theory for the size distribution of emitted dust aerosols suggests climate models underestimate the size of the global dust cycle, *P. Natl. Acad. Sci. USA*, 108, 1016–1021, <https://doi.org/10.1073/pnas.1014798108>, 2011.
- Kok, J. F., Ridley, D. A., Zhou, Q., Miller, R. L., Zhao, C., Heald, C. L., Ward, D. S., Albani, S., and Haustein, K.: Smaller desert dust cooling effect estimated from analysis of dust size and abundance, *Nat. Geosci.*, 10, 274–278, <https://doi.org/10.1038/ngeo2912>, 2017.
- Kok, J. F., Storelvmo, T., Karydis, V. A., Adebisi, A. A., Mahowald, N. M., Evan, A. T., He, C., and Leung, D. M.: Mineral dust aerosol impacts on global climate and climate change, *Nature Reviews Earth & Environment*, 4, 71–86, <https://doi.org/10.1038/s43017-022-00379-5>, 2023.
- Lafon, S., Rajot, J.-L., Alfaro, S. C., and Gaudichet, A.: Quantification of iron oxides in desert aerosol, *Atmos. Environ.*, 38, 1211–1218, <https://doi.org/10.1016/j.atmosenv.2003.11.006>, 2004.
- Lafon, S., Sokolik, I. N., Rajot, J. L., Caquineau, S., and Gaudichet, A.: Characterization of iron oxides in mineral dust aerosols: Implications for light absorption, *J. Geophys. Res.-Atmos.*, 111, D21207, <https://doi.org/10.1029/2005JD007016>, 2006.
- Lasaga, A. C., Soler, J. M., Ganor, J., Burch, T. E., and Nagy, K. L.: Chemical weathering rate laws and global geochemical cycles, *Geochim. Cosmochim. Ac.*, 58, 2361–2386, [https://doi.org/10.1016/0016-7037\(94\)90016-7](https://doi.org/10.1016/0016-7037(94)90016-7), 1994.
- Leung, D. M., Kok, J. F., Li, L., Okin, G. S., Prigent, C., Klose, M., Pérez García-Pando, C., Menut, L., Mahowald, N. M.,

- Lawrence, D. M., and Chamecki, M.: A new process-based and scale-aware desert dust emission scheme for global climate models – Part I: Description and evaluation against inverse modeling emissions, *Atmos. Chem. Phys.*, 23, 6487–6523, <https://doi.org/10.5194/acp-23-6487-2023>, 2023.
- Li, L., Mahowald, N. M., Miller, R. L., Pérez García-Pando, C., Klose, M., Hamilton, D. S., Gonçalves Ageitos, M., Ginoux, P., Balkanski, Y., Green, R. O., Kalashnikova, O., Kok, J. F., Obiso, V., Paynter, D., and Thompson, D. R.: Quantifying the range of the dust direct radiative effect due to source mineralogy uncertainty, *Atmos. Chem. Phys.*, 21, 3973–4005, <https://doi.org/10.5194/acp-21-3973-2021>, 2021.
- Li, L., Mahowald, N. M., Kok, J. F., Liu, X., Wu, M., Leung, D. M., Hamilton, D. S., Emmons, L. K., Huang, Y., Sexton, N., Meng, J., and Wan, J.: Importance of different parameterization changes for the updated dust cycle modeling in the Community Atmosphere Model (version 6.1), *Geosci. Model Dev.*, 15, 8181–8219, <https://doi.org/10.5194/gmd-15-8181-2022>, 2022.
- Li, M., Liu, H., Geng, G., Hong, C., Liu, F., Song, Y., Tong, D., Zheng, B., Cui, H., Man, H., Zhang, Q., and He, K.: Anthropogenic emission inventories in China: a review, *Natl. Sci. Rev.*, 4, 834–866, <https://doi.org/10.1093/nsr/nwx150>, 2017a.
- Li, W., Xu, L., Liu, X., Zhang, J., Lin, Y., Yao, X., Gao, H., Zhang, D., Chen, J., Wang, W., Harrison, R. M., Zhang, X., Shao, L., Fu, P., Nenes, A., and Shi, Z.: Air pollution–aerosol interactions produce more bioavailable iron for ocean ecosystems, *Science Advances*, 3, e1601749, <https://doi.org/10.1126/sciadv.1601749>, 2017b.
- Li, X., Yu, Z., Yue, M., Liu, Y., Huang, K., Chi, X., Nie, W., Ding, A., Dong, X., and Wang, M.: Impact of mineral dust photocatalytic heterogeneous chemistry on the formation of the sulfate and nitrate: A modelling study over East Asia, *Atmos. Environ.*, 316, 120166, <https://doi.org/10.1016/j.atmosenv.2023.120166>, 2024.
- Liang, L., Han, Z., Li, J., Xia, X., Sun, Y., Liao, H., Liu, R., Liang, M., Gao, Y., and Zhang, R.: Emission, transport, deposition, chemical and radiative impacts of mineral dust during severe dust storm periods in March 2021 over East Asia, *Sci. Total Environ.*, 852, 158459, <https://doi.org/10.1016/j.scitotenv.2022.158459>, 2022.
- Liu, X., Easter, R. C., Ghan, S. J., Zaveri, R., Rasch, P., Shi, X., Lamarque, J.-F., Gettelman, A., Morrison, H., Vitt, F., Conley, A., Park, S., Neale, R., Hannay, C., Ekman, A. M. L., Hess, P., Mahowald, N., Collins, W., Iacono, M. J., Bretherton, C. S., Flanner, M. G., and Mitchell, D.: Toward a minimal representation of aerosols in climate models: description and evaluation in the Community Atmosphere Model CAM5, *Geosci. Model Dev.*, 5, 709–739, <https://doi.org/10.5194/gmd-5-709-2012>, 2012.
- Liu, X., Ma, P.-L., Wang, H., Tilmes, S., Singh, B., Easter, R. C., Ghan, S. J., and Rasch, P. J.: Description and evaluation of a new four-mode version of the Modal Aerosol Module (MAM4) within version 5.3 of the Community Atmosphere Model, *Geosci. Model Dev.*, 9, 505–522, <https://doi.org/10.5194/gmd-9-505-2016>, 2016.
- Liu, Y., Dong, X., Emmons, L. K., Jo, D. S., Liu, Y., Shrivastava, M., Yue, M., Liang, Y., Song, Z., He, X., and Wang, M.: Exploring the Factors Controlling the Long-Term Trend (1988–2019) of Surface Organic Aerosols in the Continental United States by Simulations, *J. Geophys. Res.-Atmos.*, 128, e2022JD037935, <https://doi.org/10.1029/2022JD037935>, 2023.
- Long, M. C., Moore, J. K., Lindsay, K., Levy, M., Doney, S. C., Luo, J. Y., Krumhardt, K. M., Letscher, R. T., Grover, M., and Sylvester, Z. T.: Simulations With the Marine Biogeochemistry Library (MARBL), *J. Adv. Model. Earth Sy.*, 13, e2021MS002647, <https://doi.org/10.1029/2021MS002647>, 2021.
- Longo, A. F., Feng, Y., Lai, B., Landing, W. M., Shelley, R. U., Nenes, A., Mihalopoulos, N., Violaki, K., and Ingall, E. D.: Influence of Atmospheric Processes on the Solubility and Composition of Iron in Saharan Dust, *Environ. Sci. Technol.*, 50, 6912–6920, <https://doi.org/10.1021/acs.est.6b02605>, 2016.
- Luo, C., Wang, W., Sheng, L., Zhou, Y., Hu, Z., Qu, W., Li, X., and Hai, S.: Influence of polluted dust on chlorophyll-*a* concentration and particulate organic carbon in the subarctic North Pacific Ocean based on satellite observation and the WRF-Chem simulation, *Atmos. Res.*, 236, 104812, <https://doi.org/10.1016/j.atmosres.2019.104812>, 2020a.
- Luo, X., Liu, X., Pan, Y., Wen, Z., Xu, W., Zhang, L., Kou, C., Lv, J., and Goulding, K.: Atmospheric reactive nitrogen concentration and deposition trends from 2011 to 2018 at an urban site in north China, *Atmos. Environ.*, 224, 117298, <https://doi.org/10.1016/j.atmosenv.2020.117298>, 2020b.
- Mahowald, N.: Aerosol Indirect Effect on Biogeochemical Cycles and Climate, *Science*, 334, 794–796, <https://doi.org/10.1126/science.1207374>, 2011.
- Mahowald, N. M., Engelstaedter, S., Luo, C., Sealy, A., Artaxo, P., Benitez-Nelson, C., Bonnet, S., Chen, Y., Chuang, P. Y., Cohen, D. D., Dulac, F., Herut, B., Johansen, A. M., Kubilay, N., Losno, R., Maenhaut, W., Paytan, A., Prospero, J. M., Shank, L. M., and Siefert, R. L.: Atmospheric Iron Deposition: Global Distribution, Variability, and Human Perturbations, *Annu. Rev. Mar. Sci.*, 1, 245–278, <https://doi.org/10.1146/annurev.marine.010908.163727>, 2009.
- Martin, J. H.: Glacial-interglacial CO₂ change: The Iron Hypothesis, *Paleoceanography*, 5, 1–13, <https://doi.org/10.1029/PA005i001p00001>, 1990.
- Martin, J. H. and Fitzwater, S. E.: Iron deficiency limits phytoplankton growth in the north-east Pacific subarctic, *Nature*, 331, 341–343, 1988.
- Martin, J. H., Gordon, M., and Fitzwater, S. E.: The case for iron, *Limnol. Oceanogr.*, 36, 1793–1802, <https://doi.org/10.4319/lo.1991.36.8.1793>, 1991.
- Meskhidze, N., Chameides, W. L., Nenes, A., and Chen, G.: Iron mobilization in mineral dust: Can anthropogenic SO₂ emissions affect ocean productivity?, *Geophys. Res. Lett.*, 30, 2085, <https://doi.org/10.1029/2003GL018035>, 2003.
- Meskhidze, N., Chameides, W. L., and Nenes, A.: Dust and pollution: A recipe for enhanced ocean fertilization?, *J. Geophys. Res.-Atmos.*, 110, D03301, <https://doi.org/10.1029/2004JD005082>, 2005.
- Myriokefalitakis, S., Tsigaridis, K., Mihalopoulos, N., Sciare, J., Nenes, A., Kawamura, K., Segers, A., and Kanakidou, M.: In-cloud oxalate formation in the global troposphere: a 3-D modeling study, *Atmos. Chem. Phys.*, 11, 5761–5782, <https://doi.org/10.5194/acp-11-5761-2011>, 2011.
- Myriokefalitakis, S., Daskalakis, N., Mihalopoulos, N., Baker, A. R., Nenes, A., and Kanakidou, M.: Changes in dissolved

- iron deposition to the oceans driven by human activity: a 3-D global modelling study, *Biogeosciences*, 12, 3973–3992, <https://doi.org/10.5194/bg-12-3973-2015>, 2015.
- Myriokefalitakis, S., Ito, A., Kanakidou, M., Nenes, A., Krol, M. C., Mahowald, N. M., Scanza, R. A., Hamilton, D. S., Johnson, M. S., Meskhidze, N., Kok, J. F., Guieu, C., Baker, A. R., Jickells, T. D., Sarin, M. M., Bikkina, S., Shelley, R., Bowie, A., Perron, M. M. G., and Duce, R. A.: Reviews and syntheses: the GESAMP atmospheric iron deposition model intercomparison study, *Biogeosciences*, 15, 6659–6684, <https://doi.org/10.5194/bg-15-6659-2018>, 2018.
- Myriokefalitakis, S., Bergas-Massó, E., Gonçalves-Ageitos, M., Pérez García-Pando, C., van Noije, T., Le Sager, P., Ito, A., Athanasopoulou, E., Nenes, A., Kanakidou, M., Krol, M. C., and Gerasopoulos, E.: Multiphase processes in the EC-Earth model and their relevance to the atmospheric oxalate, sulfate, and iron cycles, *Geosci. Model Dev.*, 15, 3079–3120, <https://doi.org/10.5194/gmd-15-3079-2022>, 2022.
- Nickovic, S., Vukovic, A., Vujadinovic, M., Djurdjevic, V., and Pejanovic, G.: Technical Note: High-resolution mineralogical database of dust-productive soils for atmospheric dust modeling, *Atmos. Chem. Phys.*, 12, 845–855, <https://doi.org/10.5194/acp-12-845-2012>, 2012.
- O'Neill, B. C., Krieger, E., Ebi, K. L., Kemp-Benedict, E., Rihani, K., Rothman, D. S., van Ruijven, B. J., van Vuuren, D. P., Birkmann, J., Kok, K., Levy, M., and Solecki, W.: The roads ahead: Narratives for shared socioeconomic pathways describing world futures in the 21st century, *Global Environmental Change*, 42, 169–180, <https://doi.org/10.1016/j.gloenvcha.2015.01.004>, 2017.
- Ooki, A., Nishioka, J., Ono, T., and Noriki, S.: Size dependence of iron solubility of Asian mineral dust particles, *J. Geophys. Res.-Atmos.*, 114, D03202, <https://doi.org/10.1029/2008JD010804>, 2009.
- Paris, R. and Desboeufs, K. V.: Effect of atmospheric organic complexation on iron-bearing dust solubility, *Atmos. Chem. Phys.*, 13, 4895–4905, <https://doi.org/10.5194/acp-13-4895-2013>, 2013.
- Paris, R., Desboeufs, K. V., and Journet, E.: Variability of dust iron solubility in atmospheric waters: Investigation of the role of oxalate organic complexation, *Atmos. Environ.*, 45, 6510–6517, <https://doi.org/10.1016/j.atmosenv.2011.08.068>, 2011.
- Pye, H. O. T., Nenes, A., Alexander, B., Ault, A. P., Barth, M. C., Clegg, S. L., Collett Jr., J. L., Fahey, K. M., Hennigan, C. J., Herrmann, H., Kanakidou, M., Kelly, J. T., Ku, I.-T., McNeill, V. F., Riemer, N., Schaefer, T., Shi, G., Tilgner, A., Walker, J. T., Wang, T., Weber, R., Xing, J., Zaveri, R. A., and Zuend, A.: The acidity of atmospheric particles and clouds, *Atmos. Chem. Phys.*, 20, 4809–4888, <https://doi.org/10.5194/acp-20-4809-2020>, 2020.
- Rathod, S. D., Hamilton, D. S., Mahowald, N. M., Klimont, Z., Corbett, J. J., and Bond, T. C.: A Mineralogy-Based Anthropogenic Combustion-Iron Emission Inventory, *J. Geophys. Res.-Atmos.*, 125, e2019JD032114, <https://doi.org/10.1029/2019JD032114>, 2020.
- Reichard, P. U., Kraemer, S. M., Frazier, S. W., and Kretzschmar, R.: Goethite Dissolution in the Presence of Phytosiderophores: Rates, Mechanisms, and the Synergistic Effect of Oxalate, *Plant Soil*, 276, 115–132, <https://doi.org/10.1007/s11104-005-3504-9>, 2005.
- Ruan, X., Zhao, C., Zaveri, R. A., He, P., Wang, X., Shao, J., and Geng, L.: Simulations of aerosol pH in China using WRF-Chem (v4.0): sensitivities of aerosol pH and its temporal variations during haze episodes, *Geosci. Model Dev.*, 15, 6143–6164, <https://doi.org/10.5194/gmd-15-6143-2022>, 2022.
- Sakata, K., Kurisu, M., Takeichi, Y., Sakaguchi, A., Tanimoto, H., Tamenori, Y., Matsuki, A., and Takahashi, Y.: Iron (Fe) speciation in size-fractionated aerosol particles in the Pacific Ocean: The role of organic complexation of Fe with humic-like substances in controlling Fe solubility, *Atmos. Chem. Phys.*, 22, 9461–9482, <https://doi.org/10.5194/acp-22-9461-2022>, 2022.
- Sathyendranath, S., Brewin, R. J. W., Brockmann, C., Brotas, V., Calton, B., Chuprin, A., Cipollini, P., Couto, A. B., Dingle, J., Doerffer, R., Donlon, C., Dowell, M., Farman, A., Grant, M., Groom, S., Horseman, A., Jackson, T., Krasemann, H., Lavender, S., Martinez-Vicente, V., Mazeran, C., Mélin, F., Moore, T. S., Müller, D., Regner, P., Roy, S., Steele, C. J., Steinmetz, F., Swinton, J., Taberner, M., Thompson, A., Valente, A., Zühlke, M., Brando, V. E., Feng, H., Feldman, G., Franz, B. A., Frouin, R., Gould, R. W., Hooker, S. B., Kahru, M., Kratzer, S., Mitchell, B. G., Muller-Karger, F. E., Sosik, H. M., Voss, K. J., Werdel, J., and Platt, T.: An Ocean-Colour Time Series for Use in Climate Studies: The Experience of the Ocean-Colour Climate Change Initiative (OC-CCI), *Sensors*, 19, 4285, 2019.
- Scanza, R. A., Mahowald, N., Ghan, S., Zender, C. S., Kok, J. F., Liu, X., Zhang, Y., and Albani, S.: Modeling dust as component minerals in the Community Atmosphere Model: development of framework and impact on radiative forcing, *Atmos. Chem. Phys.*, 15, 537–561, <https://doi.org/10.5194/acp-15-537-2015>, 2015.
- Scanza, R. A., Hamilton, D. S., Perez Garcia-Pando, C., Buck, C., Baker, A., and Mahowald, N. M.: Atmospheric processing of iron in mineral and combustion aerosols: development of an intermediate-complexity mechanism suitable for Earth system models, *Atmos. Chem. Phys.*, 18, 14175–14196, <https://doi.org/10.5194/acp-18-14175-2018>, 2018.
- Shi, J., Guan, Y., Ito, A., Gao, H., Yao, X., Baker, A. R., and Zhang, D.: High Production of Soluble Iron Promoted by Aerosol Acidification in Fog, *Geophys. Res. Lett.*, 47, e2019GL086124, <https://doi.org/10.1029/2019GL086124>, 2020.
- Shi, J., Guan, Y., Gao, H., Yao, X., Wang, R., and Zhang, D.: Aerosol Iron Solubility Specification in the Global Marine Atmosphere with Machine Learning, *Environ. Sci. Technol.*, 56, 16453–16461, <https://doi.org/10.1021/acs.est.2c05266>, 2022.
- Shi, Z., Bonneville, S., Krom, M. D., Carslaw, K. S., Jickells, T. D., Baker, A. R., and Benning, L. G.: Iron dissolution kinetics of mineral dust at low pH during simulated atmospheric processing, *Atmos. Chem. Phys.*, 11, 995–1007, <https://doi.org/10.5194/acp-11-995-2011>, 2011a.
- Shi, Z., Krom, M. D., Bonneville, S., Baker, A. R., Bristow, C., Drake, N., Mann, G., Carslaw, K., McQuaid, J. B., Jickells, T., and Benning, L. G.: Influence of chemical weathering and aging of iron oxides on the potential iron solubility of Saharan dust during simulated atmospheric processing, *Global Biogeochem. Cy.*, 25, GB2010, <https://doi.org/10.1029/2010GB003837>, 2011b.
- Shi, Z., Krom, M. D., Jickells, T. D., Bonneville, S., Carslaw, K. S., Mihalopoulos, N., Baker, A. R., and Benning, L. G.: Impacts on iron solubility in the mineral dust by processes in the source region and the atmosphere: A review, *Aeolian Res.*, 5, 21–42, <https://doi.org/10.1016/j.aeolia.2012.03.001>, 2012.

- Spokes, L. J. and Jickells, T. D.: Factors controlling the solubility of aerosol trace metals in the atmosphere and on mixing into seawater, *Aquat. Geochem.*, 1, 355–374, <https://doi.org/10.1007/BF00702739>, 1995.
- Storelvmo, T.: Aerosol Effects on Climate via Mixed-Phase and Ice Clouds, *Annu. Rev. Earth Pl. Sc.*, 45, 199–222, <https://doi.org/10.1146/annurev-earth-060115-012240>, 2017.
- Takeda, S. and Tsuda, A.: An in situ iron-enrichment experiment in the western subarctic Pacific (SEEDS): Introduction and summary, *Prog. Oceanogr.*, 64, 95–109, <https://doi.org/10.1016/j.pocean.2005.02.004>, 2005.
- Tilmes, S., Hodzic, A., Emmons, L. K., Mills, M. J., Gettelman, A., Kinnison, D. E., Park, M., Lamarque, J.-F., Vitt, F., Shrivastava, M., Campuzano-Jost, P., Jimenez, J. L., and Liu, X.: Climate Forcing and Trends of Organic Aerosols in the Community Earth System Model (CESM2), *J. Adv. Model. Earth Sy.*, 11, 4323–4351, <https://doi.org/10.1029/2019MS001827>, 2019.
- Wang, J., Gui, H., An, L., Hua, C., Zhang, T., and Zhang, B.: Modeling for the source apportionments of PM₁₀ during sand and dust storms over East Asia in 2020, *Atmos. Environ.*, 267, 118768, <https://doi.org/10.1016/j.atmosenv.2021.118768>, 2021.
- Westberry, T. K., Behrenfeld, M. J., Shi, Y. R., Yu, H., Remer, L. A., and Bian, H.: Atmospheric nourishment of global ocean ecosystems, *Science*, 380, 515–519, <https://doi.org/10.1126/science.abq5252>, 2023.
- Wu, C., Lin, Z., Shao, Y., Liu, X., and Li, Y.: Drivers of recent decline in dust activity over East Asia, *Nat. Commun.*, 13, 7105, <https://doi.org/10.1038/s41467-022-34823-3>, 2022.
- Wu, M., Liu, X., Yu, H., Wang, H., Shi, Y., Yang, K., Darmenov, A., Wu, C., Wang, Z., Luo, T., Feng, Y., and Ke, Z.: Understanding processes that control dust spatial distributions with global climate models and satellite observations, *Atmos. Chem. Phys.*, 20, 13835–13855, <https://doi.org/10.5194/acp-20-13835-2020>, 2020.
- Xu, C., Guan, Q., Lin, J., Luo, H., Yang, L., Tan, Z., Wang, Q., Wang, N., and Tian, J.: Spatiotemporal variations and driving factors of dust storm events in northern China based on high-temporal-resolution analysis of meteorological data (1960–2007), *Environ. Pollut.*, 260, 114084, <https://doi.org/10.1016/j.envpol.2020.114084>, 2020.
- Xu, N. and Gao, Y.: Characterization of hematite dissolution affected by oxalate coating, kinetics and pH, *Appl. Geochem.*, 23, 783–793, <https://doi.org/10.1016/j.apgeochem.2007.12.026>, 2008.
- Yang, T., Ma, X., and Zhao, J.: Long-term trends of aerosol and cloud fraction over Eastern China based on ground-based observations, *Atmos. Environ.*, 309, 119954, <https://doi.org/10.1016/j.atmosenv.2023.119954>, 2023.
- Yoon, J.-E., Kim, K., Macdonald, A. M., Park, K.-T., Kim, H.-C., Yoo, K.-C., Yoon, H.-I., Yang, E. J., Jung, J., Lim, J.-H., Kim, J.-H., Lee, J., Choi, T.-J., Song, J.-M., and Kim, I.-N.: Spatial and temporal variabilities of spring Asian dust events and their impacts on chlorophyll-*a* concentrations in the western North Pacific Ocean, *Geophys. Res. Lett.*, 44, 1474–1482, <https://doi.org/10.1002/2016GL072124>, 2017.
- Yue, M., Dong, X., Wang, M., Emmons, L. K., Liang, Y., Tong, D., Liu, Y., and Liu, Y.: Modeling the Air Pollution and Aerosol-PBL Interactions Over China Using a Variable-Resolution Global Model, *J. Geophys. Res.-Atmos.*, 128, e2023JD039130, <https://doi.org/10.1029/2023JD039130>, 2023.
- Zan, J., Maher, Barbara A., Yamazaki, T., Fang, X., Han, W., Kang, J., and Hu, Z.: Mid-Pleistocene links between Asian dust, Tibetan glaciers, and Pacific iron fertilization, *P. Natl. Acad. Sci. USA*, 120, e2304773120, <https://doi.org/10.1073/pnas.2304773120>, 2023.
- Zaveri, R. A., Easter, R. C., and Peters, L. K.: A computationally efficient Multicomponent Equilibrium Solver for Aerosols (MESA), *J. Geophys. Res.-Atmos.*, 110, D24203, <https://doi.org/10.1029/2004JD005618>, 2005a.
- Zaveri, R. A., Easter, R. C., and Wexler, A. S.: A new method for multicomponent activity coefficients of electrolytes in aqueous atmospheric aerosols, *J. Geophys. Res.-Atmos.*, 110, D02201, <https://doi.org/10.1029/2004JD004681>, 2005b.
- Zaveri, R. A., Easter, R. C., Fast, J. D., and Peters, L. K.: Model for Simulating Aerosol Interactions and Chemistry (MOSAIC), *J. Geophys. Res.-Atmos.*, 113, D13204, <https://doi.org/10.1029/2007JD008782>, 2008.
- Zaveri, R. A., Easter, R. C., Singh, B., Wang, H., Lu, Z., Tilmes, S., Emmons, L. K., Vitt, F., Zhang, R., Liu, X., Ghan, S. J., and Rasch, P. J.: Development and Evaluation of Chemistry-Aerosol-Climate Model CAM5-ChemMAM7-MOSAIC: Global Atmospheric Distribution and Radiative Effects of Nitrate Aerosol, *J. Adv. Model. Earth Sy.*, 13, e2020MS002346, <https://doi.org/10.1029/2020MS002346>, 2021.
- Zender, C. S., Bian, H., and Newman, D.: Mineral Dust Entrainment and Deposition (DEAD) model: Description and 1990s dust climatology, *J. Geophys. Res.-Atmos.*, 108, 4416, <https://doi.org/10.1029/2002JD002775>, 2003a.
- Zender, C. S., Newman, D., and Torres, O.: Spatial heterogeneity in aeolian erodibility: Uniform, topographic, geomorphic, and hydrologic hypotheses, *J. Geophys. Res.-Atmos.*, 108, 4543, <https://doi.org/10.1029/2002JD003039>, 2003b.
- Zhang, H., Li, R., Huang, C., Li, X., Dong, S., Wang, F., Li, T., Chen, Y., Zhang, G., Ren, Y., Chen, Q., Huang, R., Chen, S., Xue, T., Wang, X., and Tang, M.: Seasonal variation of aerosol iron solubility in coarse and fine particles at an inland city in northwestern China, *Atmos. Chem. Phys.*, 23, 3543–3559, <https://doi.org/10.5194/acp-23-3543-2023>, 2023a.
- Zhang, T., Zheng, M., Sun, X., Chen, H., Wang, Y., Fan, X., Pan, Y., Quan, J., Liu, J., Wang, Y., Lyu, D., Chen, S., Zhu, T., and Chai, F.: Environmental impacts of three Asian dust events in the northern China and the northwestern Pacific in spring 2021, *Sci. Total Environ.*, 859, 160230, <https://doi.org/10.1016/j.scitotenv.2022.160230>, 2023b.
- Zhao, W., Wang, Z., Li, S., Li, L., Wei, L., Xie, Q., Yue, S., Li, T., Liang, Y., Sun, Y., Wang, Z., Li, X., Kawamura, K., Wang, T., and Fu, P.: Water-soluble low molecular weight organics in cloud water at Mt. Tai Mo Shan, Hong Kong, *Sci. Total Environ.*, 697, 134095, <https://doi.org/10.1016/j.scitotenv.2019.134095>, 2019.
- Zheng, B., Tong, D., Li, M., Liu, F., Hong, C., Geng, G., Li, H., Li, X., Peng, L., Qi, J., Yan, L., Zhang, Y., Zhao, H., Zheng, Y., He, K., and Zhang, Q.: Trends in China's anthropogenic emissions since 2010 as the consequence of clean air actions, *Atmos. Chem. Phys.*, 18, 14095–14111, <https://doi.org/10.5194/acp-18-14095-2018>, 2018.

Zhou, M., Zheng, G., Wang, H., Qiao, L., Zhu, S., Huang, D., An, J., Lou, S., Tao, S., Wang, Q., Yan, R., Ma, Y., Chen, C., Cheng, Y., Su, H., and Huang, C.: Long-term trends and drivers of aerosol pH in eastern China, *Atmos. Chem. Phys.*, 22, 13833–13844, <https://doi.org/10.5194/acp-22-13833-2022>, 2022.

Zhu, Y., Li, W., Lin, Q., Yuan, Q., Liu, L., Zhang, J., Zhang, Y., Shao, L., Niu, H., Yang, S., and Shi, Z.: Iron solubility in fine particles associated with secondary acidic aerosols in east China, *Environ. Pollut.*, 264, 114769, <https://doi.org/10.1016/j.envpol.2020.114769>, 2020.